JET (^{3}He)–D scenarios relying on RF heating: survey of selected recent experiments

2009 Plasma Phys. Control. Fusion 51 044007

(http://iopscience.iop.org/0741-3335/51/4/044007)

Plasma Phys. Control. Fusion **51** (2009) 044007 (31pp) doi:10.1088/0741-3335/51/4/044007

JET (^{3}He)–D scenarios relying on RF heating: survey of selected recent experiments

D Van Eester[1,2], E Lerche[1,2], Y Andrew[1,3], T M Biewer[1,4], A Casati[1,5], K Crombé[1,6], E de la Luna[1,7], G Ericsson[1,8], R Felton[1,3], L Giacomelli[1,8], C Giroud[1,3], N Hawkes[1,3], C Hellesen[1,8], A Hjalmarsson[1,8], E Joffrin[1,5], J Källne[1,9], V Kiptily[1,3], P Lomas[1,3], P Mantica[1,10], A Marinoni[1,11], M-L Mayoral[1,3], J Ongena[1,2], M-E Puiatti[1,12], M Santala[1,3], S Sharapov[1,3], M Valisa[1,12] and JET EFDA contributors[1,13]

[1] JET-EFDA Culham Science Centre, Abingdon, OX14 3DB, UK
[2] Laboratory for Plasma Physics-ERM/KMS, TEC Partner, Brussels, Belgium
[3] Euratom-UKAEA Fusion Association, Culham Science Centre, UK
[4] Oak Ridge National Laboratory, Oak Ridge, TN 37831, USA
[5] CEA/DRFC Assoc. Euratom-CEA, Cadarache, France
[6] Department of Applied Physics, Ghent University, Ghent, Belgium
[7] Laboratorio Nacional de Fusion, Asociación EURATOM-CIEMAT, CIEMAT, Madrid, Spain
[8] Department of Physics and Astronomy, Uppsala University, Uppsala, Sweden
[9] Department of Engineering Sciences, Uppsala University, Uppsala, Sweden
[10] Istituto di Fisica del Plasma, Assoc. Euratom-ENEA-CNR, Milano, Italy
[11] CRPP-EPFL, Assoc. Euratom Confédération Suisse, CH-1015, Lausanne, Switzerland
[12] Consorzio RFX, Euratom-ENEA Association, Padova, Italy

Received 17 July 2008, in final form 30 August 2008
Published 18 March 2009
Online at stacks.iop.org/PPCF/51/044007

Abstract

Recent JET experiments have been devoted to the study of (^{3}He)–D plasmas involving radio frequency (RF) heating. This paper starts by discussing the RF heating efficiency theoretically expected in such plasmas, covering both relevant aspects of wave and of particle dynamics. Then it gives a concise summary of the main conclusions drawn from recent experiments that were either focusing on studying RF heating physics aspects or that were adopting RF heating as a tool to study plasma behavior. Depending on the minority concentration chosen, different physical phenomena are observed. At very low concentration ($X[^3\mathrm{He}] < 1\%$), energetic tails are formed which trigger MHD activity and result in loss of fast particles. Alfvén cascades were observed and gamma ray tomography indirectly shows the impact of sawtooth crashes on the fast particle orbits. Low concentration ($X[^3\mathrm{He}] < 10\%$) favors minority heating while for $X[^3\mathrm{He}] \gg 10\%$ electron mode conversion damping becomes dominant. Evidence for the Fuchs *et al* standing wave effect (Fuchs *et al* 1995 *Phys. Plasmas* **2** 1637–47) on the absorption is presented. RF induced

[13] See the appendix of M L Watkins *et al* 2006 *Proc. 21st Int. Conf. on Fusion Energy 2006 (Chengdu, China, 2006)* (Vienna: IAEA).

deuterium tails were observed in mode conversion experiments with large $X[^3\mathrm{He}]$ ($\approx$18%). As tentative modeling shows, the formation of these tails can be explained as a consequence of wave power absorption by neutral beam particles that efficiently interact with the waves well away from the cold D cyclotron resonance position as a result of their substantial Doppler shift. As both ion and electron RF power deposition profiles in (^{3}He)–D plasmas are fairly narrow—giving rise to localized heat sources—the RF heating method is an ideal tool for performing transport studies. Various of the experiments discussed here were done in plasmas with internal transport barriers (ITBs). ITBs are identified as regions with locally reduced diffusivity, where poloidal spinning up of the plasma is observed. The present know-how on the role of RF heating for impurity transport is also briefly summarized.

(Some figures in this article are in colour only in the electronic version)

1. Introduction: Why doing ^{3}He experiments?

For experiments with ion cyclotron resonance heating (ICRH), using ^{3}He as a minority gas has a number of advantages. Because of its relatively high mass, it is more difficult to heat ^{3}He than the most commonly used minority gas—H—to high energies. Hence radio frequency (RF) heated tails are less likely to form for a given amount of coupled RF power. Also, the critical velocity (at which the fraction of power collisionally transferred to the bulk electrons equals the power passed on to the ions) of ^{3}He is several hundred kiloelectronvolts high. For both these reasons, the power transferred from the heated minority to the bulk commonly ends up in the ion channel rather than in the electron channel. Increasing the minority concentration results in fading out the minority heating and fading in mode conversion heating, which allows creating a highly localized electron heat source through the very efficient electron absorption that the essentially electrostatic ion Bernstein wave undergoes as soon as it is excited near the ion–ion hybrid resonance layer. Both in the minority and in the mode conversion heating schemes relatively narrow power deposition profiles are obtained: ^{3}He ions stick much closer to a magnetic surface because—in contrast to H—their limited energy does not give rise to wide banana orbits. The modest width of the deposition is also due to the electron damping being very sensitive to the electric field gradients, i.e. to the magnitude of the wave vector which increases dramatically very close to the mode conversion point. Hence, both heating regimes offer suitable heat sources for dedicated transport studies, the electron and ion channel being separated depending on the choice of the minority concentration and provided the density is not too high to avoid fast equipartition, and the depositions being fairly localized. Moreover, because RF tails are not likely to form unless the minority concentration is purposely kept extremely low, MHD modes excited by fast particles are less of an issue in (^{3}He) plasmas. Since, for example, sawteeth often compromise the interpretation of the dynamics of temperature in response to the auxiliary power (adding effects occurring on a time scale much faster than that of the modulation, thus blurring the simple cause–effect relation between heat source, the relatively slow diffusion-dominated heat transport and the temperature response), this lack of MHD activity is much desired when probing the plasma to learn about transport.

Aside from the advantages ^{3}He has from the plasma physics study point of view, ^{3}He has a crucial role to play in the next step device: it is one of the gases envisaged to be used in the

non-activated stage of ITER and it will be a crucial plasma constituent during the machine's activated life phase during which it will indirectly heat the bulk ions and thereby crank up the fusion yield when the RF ion heating scheme foreseen for ITER (tritium heating at its second cyclotron harmonic frequency) is adopted. Estimates predict that adding a few percent of ^{3}He gas to a balanced D–T ITER gas mixture gives rise to a doubling of the neutron yield for the foreseen 40 MW of ICRH on the machine (see, e.g. [1] and the references therein). The role of ^{3}He in D–T plasmas was experimentally tested in JET [2].

Theoretical predictions reveal that—for typical JET conditions—optimal ^{3}He minority heating in D plasmas occurs at ^{3}He concentrations $X[^3\mathrm{He}] = N_{^3\mathrm{He}}/N_\mathrm{e}$ of about 8% while electron 'mode conversion' damping on short wavelength waves near the ion–ion hybrid layer requires $X[^3\mathrm{He}] \approx 20\%$. Three interesting experimental regimes can then be distinguished for (^{3}He)–D plasmas:

(1) the mode conversion regime which is optimal for performing electron heat studies,
(2) the minority heating scheme which allows probing plasmas for ion transport and
(3) the regime of very low ^{3}He concentrations during which RF power allows one to trigger MHD activity through excitation of Alfvén modes extracting energy from the RF heated fast particle population(s).

All three regimes have been examined in JET recently and some of the obtained results are the subject of this paper. Only 'standard' heating scenarios are reported on here. These are scenarios for which the majority's charge to mass number ratio Z/A is smaller than that of the minority. This moves the fast-to-Bernstein-wave mode conversion layer towards the high field side when the minority concentration is increased. So-called 'inverted' scenario's have $(Z/A)_\mathrm{majority} > (Z/A)_\mathrm{minority}$, which not only causes the mode conversion layer to shift towards the low rather than to the high field side for increasing minority concentrations but are also characterized by a much lower concentration (merely a few per cent) at which the mode conversion regime is reached. This latter regime was extensively discussed in [3].

Transport studies require localized heat sources and rely on the effect of these heat sources being detected via detailed temperature (and strictly also density) response studies. This is typically done by modulating the auxiliary heating power, which causes the temperature time traces to 'break' $\partial T/\partial t_\mathrm{pre} \neq \partial T/\partial t_\mathrm{post}$ every time the power level is abruptly changed. A suitable modulation frequency is always a compromise: at too low frequency, the instantaneous dynamics is blurred as undesired phenomena occurring on a long time scale mix in with the studied instantaneous response to the power change, while at too high frequency the magnitude of the temperature response is often too small to be discerned from the signal noise, and the statistical relevance becomes questionable because of the diagnostic sampling rate. In JET a modulation frequency of the RF power of $\approx$20 Hz is frequently used for electron transport studies. Ion transport studies not only require a lower modulation frequency ($\approx$6 Hz) but also a more sophisticated analysis since the ion response is slower, the collisional slowing down time of fast particles typically being a few hundred milliseconds. Hence the simple 'breaking' of the bulk ion temperature is not only mixed up by the indirect heating via the fast minority that is slowing down: the essentially linear behavior characteristic for fast modulation is replaced by a saturation prior to and an exponential decay after the break (see, e.g. [4]).

This paper sums up a number of key findings of JET experiments relying on RF heating which were recently performed in plasmas containing ^{3}He. As analysis of the available data for several of the ^{3}He experiments is still ongoing and further experiments will be required to reach firm conclusions, the goal of the paper is to summarize the present knowledge. For topics that have reached maturity, the paper compiles the existing literature which can be consulted. The first section is devoted to preliminary modeling of RF heating of (^{3}He)–D

plasmas, giving a flavor of the role of the various species in different circumstances and pointing out some subtleties in the evaluation of the RF power deposition. Then some short notes are provided on the adopted tools e.g. on the real time control scheme used for keeping the minority concentration fixed. The link between RF heating, fast particles and MHD activity is the first of these topics. Next, a study of the role of standing wave patterns in enhancing RF wave damping is made. The role of RF heating in creating fast energy beam particles is a third topic. After that, the probing of ITBs relying on RF power is discussed. Finally, a very brief section gives an overview of the present understanding of the potential of RF heating to prevent impurity accumulation in the plasma.

A vast amount of literature has been published on the impact of RF heating in JET plasmas. This paper focuses on some of the more recent findings, but the interested reader is referred to the paper of Noterdaeme *et al* [5] and the references therein for a more extensive overview.

2. RF heating (^{3}He)–D plasmas: modeling

2.1. Wave propagation and damping aspects

To get a first impression of how RF waves interact with (^{3}He)–D plasmas, the TOMCAT wave equation solver [6] was used. All shown results assume that a pure fast wave is incident on the plasma from the low magnetic field side. The computation provides the field and the corresponding absorption for a double sweep of the wave over the plasma (from the launching point to either the high field side fast wave cutoff or the cutoff/confluence pair close to $\omega = \Omega_{^3\mathrm{He}}$). TOMCAT is a 1D wave code that solves a 12th order wave equation system, retaining the toroidal curvature of the tokamak but omitting the poloidal magnetic field and incorporating up to dominant 3rd harmonic cyclotron heating effects. It retains up to second order Larmor radius terms in the operator either acting on the electric field or on the test function vector in the weak Galerkin form of the wave equation and hence has up to 4th order Larmor radius terms and 4th derivatives acting on each of the electric field components in the corresponding dielectric tensor, raising the order of the wave system from the usual 6 to 12 but guaranteeing a positive definite and purely resonant absorption for Maxwellian populations for any of the retained waves. The drawback that all plasma constituents are assumed to be Maxwellian will be commented on when describing RF heating of beam particles as it requires a more sophisticated tool to be used when seeking more robust answers than the ones presented in this section on 1D modeling. The imposed boundary conditions correspond to a pure excitation of 1 (here the incoming fast wave) of the 12 modes described by the system. All other wave solutions capable of carrying power into the integration domain are forced to be zero. No condition whatsoever is imposed on the modes carrying power out of the domain of interest so, besides the power deposition profile, the program provides all connection (reflection, transmission and mode conversion) coefficients of all modes that can be excited in the plasma. Note that, by construction and opposite to what is more traditionally done when including the antenna in the model, the incoming power does not need to be totally absorbed. The difference between the launched and the total absorbed power in a double transit gives an idea of the absorption efficiency of the studied RF heating scenario. As the aim of this section is only to sketch qualitatively how and where wave power is expected to be absorbed, the adopted CPU nonintensive 1D model is adequate. But many effects are outside its scope. Various authors contributed to include 2D or even 3D effects in wave equation solvers. The interested reader is referred to the works of Brambilla (see, e.g. [7] and the references therein), Jaeger [8], Popovitch [9] and Vdovin [10] to name just a few.

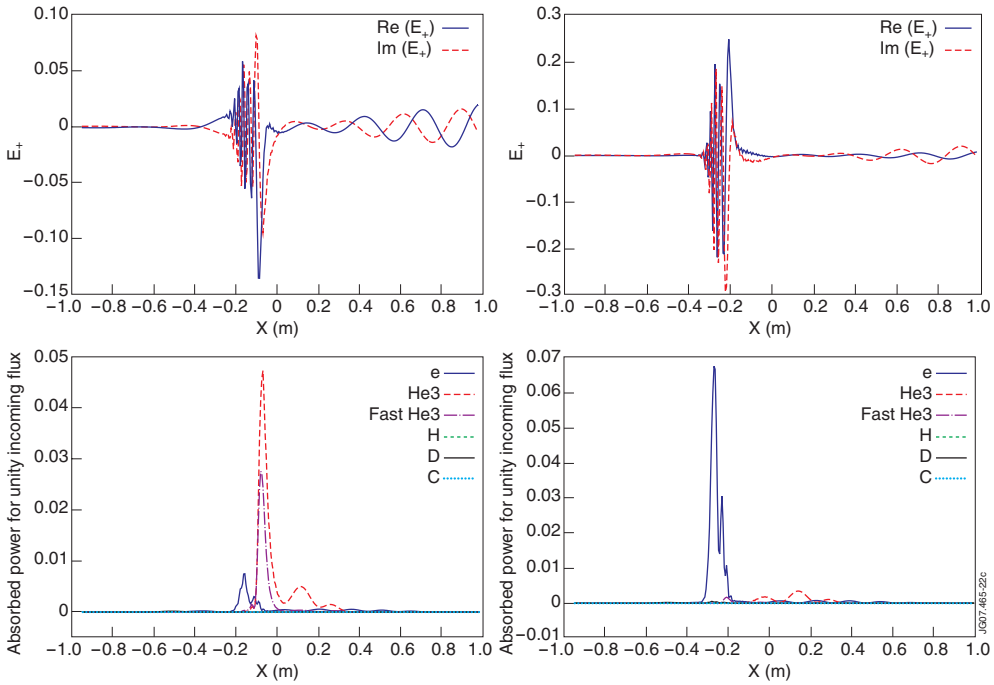

Figure 1. Electric field structure of the field circular polarization component rotating with the ions (top) and power deposition profile (bottom) for predominant minority (10% ^{3}He; left) and mode conversion (20% ^{3}He; right) heating. The quantities are plotted as a function of x, the distance from the geometric center: $x = R - R_o$. An analytical equilibrium [6] has been adopted. Note that the dominant absorption shifts position as the efficiency of the competing absorption mechanisms changes due to the fact that the local wave polarization dependences on the minority concentration. The second ^{3}He subpopulation has a concentration of 1% and a temperature of 20 keV.

Around $B_o \sim 3.45$ T, the JET ICRH system can operate at two frequencies to guarantee core ^{3}He heating: the cold (non-Doppler shifted) cyclotron layer of ^{3}He can be positioned at 0.15–0.20 m from the plasma center on the low or the high field side using $f = 33$ MHz and $f = 37$ MHz, respectively. A slight reduction of the magnetic field shifts the former to the plasma center and the latter to the high field side. The top subfigure in figure 1 depicts the wave pattern of the left rotating component of the electric field E_+—responsible for minority heating of thermal ^{3}He ions—for a (^{3}He)–D plasma with $X[^3\text{He}] = 10\%$ (left) and 20% (right), respectively. A fast wave approaches the plasma core from the low field side (from the right on the figure) and hits the ^{3}He cyclotron damping layer and the mode conversion layer. At the ion–ion hybrid (conversion) layer, the wave becomes a superposition of a long wavelength fast and a short wavelength ion Bernstein wave; the latter is damped relatively close to the region where it was excited. The corresponding power deposition profiles are depicted underneath the respective electric field components. At the lower concentration ion heating dominates the electron heating while at the higher concentration it is the other way around.

Ion or electron heating are never exclusively present, though. For typical parameters relevant for the JET experiments described here ($B_o = 3.35$ T, central density $N_{e,o} = 3.5 \times 10^{19}$ m^{-3}, edge density $N_{e,s} = 1.5 \times 10^{19}$ m^{-3}, central electron temperature $T_{e,o} = 8$ keV, central ion temperature $T_{i,o} = 10$ keV, edge temperature $T_{i,s} = T_{e,s} = 1$ keV, RF frequency $f = 33$ MHz, toroidal mode number $n = 27$ typical for dipole phasing of the antenna,

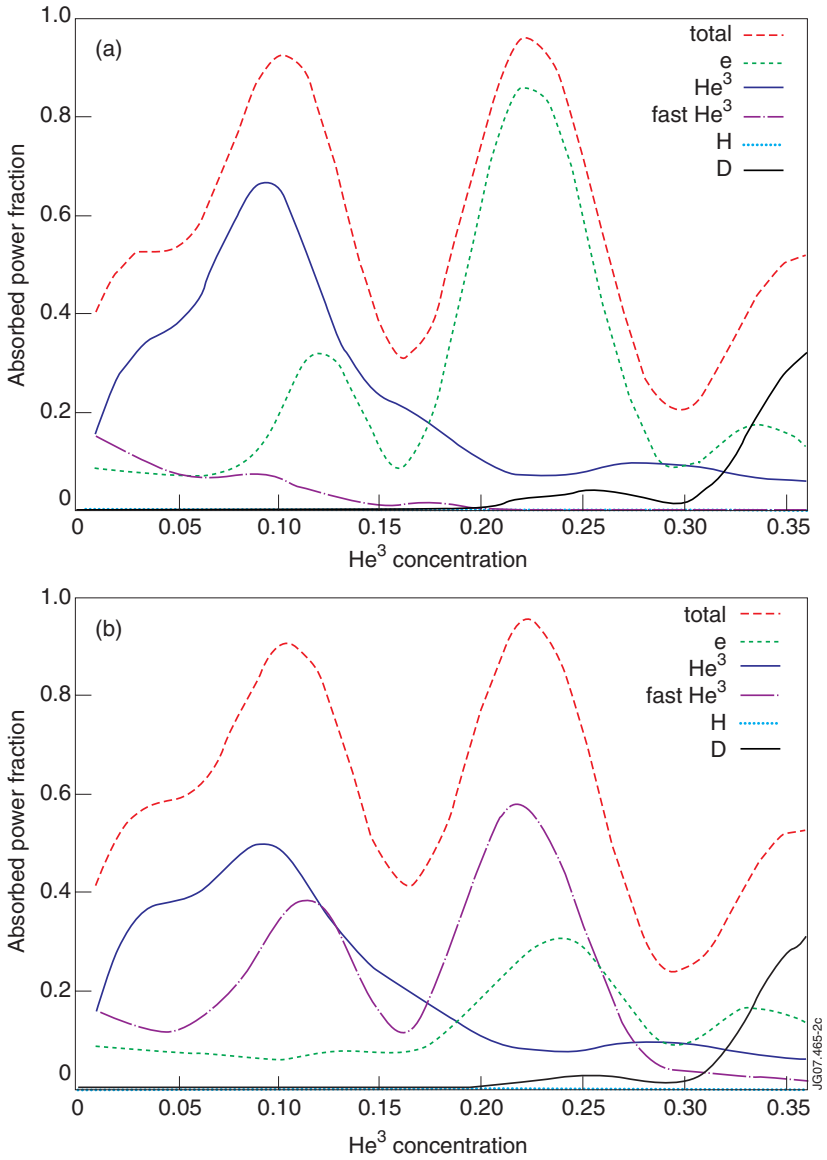

Figure 2. Fraction of the launched wave power absorbed in a double pass over the plasma as a function of the ^{3}He concentration in a (^{3}He)–D plasma containing a fast subpopulation of ^{3}He ions. Two cases are considered: (*a*) all ion species—including the subclass of 1% of ^{3}He particles labelled as 'fast ^{3}He'—are assumed thermal, sharing the same core temperature of $T_o = 10$ keV, (*b*) thermal ions are considered but now this 1% of fast ^{3}He ions has a central temperature of $T_o = 100$ keV.

$X[\mathrm{H}] = N_\mathrm{H}/N_\mathrm{e} = 1\%$ and $X[\mathrm{C}] = N_\mathrm{C}/N_\mathrm{e} = 2\%$ from interaction of the plasma with the wall), one finds that the ion heating is maximal at $X[^3\mathrm{He}] \approx 8\%$ while the electron heating is maximal at $X[^3\mathrm{He}] \approx 22\%$ (top figure in figure 2) when all populations are thermal. As soon a ^{3}He tail forms, the ^{3}He damping competes with the damping on the electrons. The bottom figure in figure 2 shows that substituting as little as 1% of the thermal ^{3}He by fast ^{3}He having an

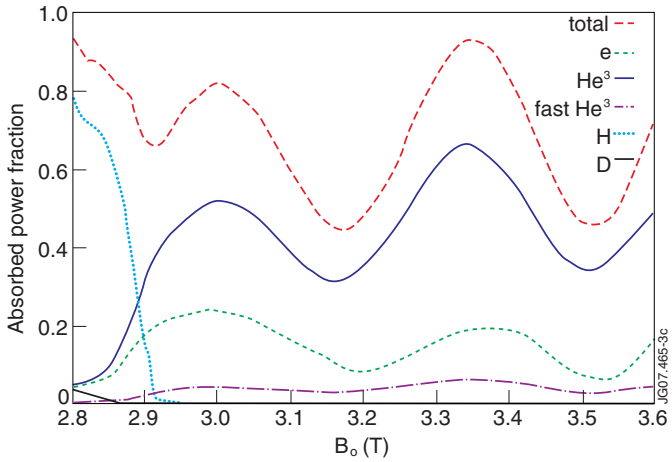

Figure 3. Fraction of the launched wave power absorbed in a double pass over the plasma as a function of the toroidal magnetic field strength; $X[^3\mathrm{He}] = 10\%$ and other parameters as for the thermal plasma (see the main text and caption of figure 2(*a*)).

effective temperature of 100 keV, the mode conversion efficiency is dramatically diminished. It is interesting to note that the total absorbed power is very similar in the two shown cases but that the redistribution of the power is different.

Rather significant power densities are required to form a high-energy subpopulation: when $X[^3\mathrm{He}] = 10\%$ and for a local temperature of 10 keV for all background species, it takes power densities of the order of 0.5–0.6 MW m^{-3} to attain fast ^{3}He temperatures of the order of 100 keV while for $X[^3\mathrm{He}] = 20\%$ the same power densities only allow one to get $T_{\mathrm{fast}} = 50$ keV. Hence efficient fully central RF power deposition and a low enough ^{3}He concentration are required to create an even moderate ^{3}He tail in JET at the typical plasma densities adopted.

Note that the total absorption has an oscillatory behavior as a function of the minority concentration in figure 2: although the partitioning of the absorbed power among the various species differs depending on the temperature of the fast ^{3}He, the total absorption peaks at about $X[^3\mathrm{He}] = 10\%$ and at about $X[^3\mathrm{He}] = 22\%$, a third peak manifesting itself beyond $X[^3\mathrm{He}] = 35\%$. This is interpreted as a bounded plasma (standing wave) effect, first identified in [11] and associated with a constructive/destructive interference of the fast waves traveling towards and from the high field side cutoff. Fuchs *et al* proposed exploiting this effect to make mode conversion heating more efficient since it manifested itself in their (absorption-less) model as an interference effect between the fast wave cutoff and the mode conversion point, allowing to have higher electric field values at the mode conversion location and thus a bigger power transfer to the mode converted branch when an integer number of wavelengths can be folded in between the high field side cutoff and the confluence point. If this interpretation of the standing wave effect is the correct one, one would expect it to show up in a scan of any of the parameters changing either the relative distance of these two points (e.g. B_o or $X[^3\mathrm{He}]$), or the fast wave wavelength (e.g. the RF frequency or the plasma density). Figure 3 shows that the same effect is indeed observed when making a scan of the toroidal magnetic field, which displaces the ion–ion hybrid location at fixed frequency; all parameters are as before while a fixed $X[^3\mathrm{He}] = 10\%$ is assumed. At lower magnetic field values another dominant absorber enters the physical picture: H minority heating at the low field side becomes the dominant heating mechanism.

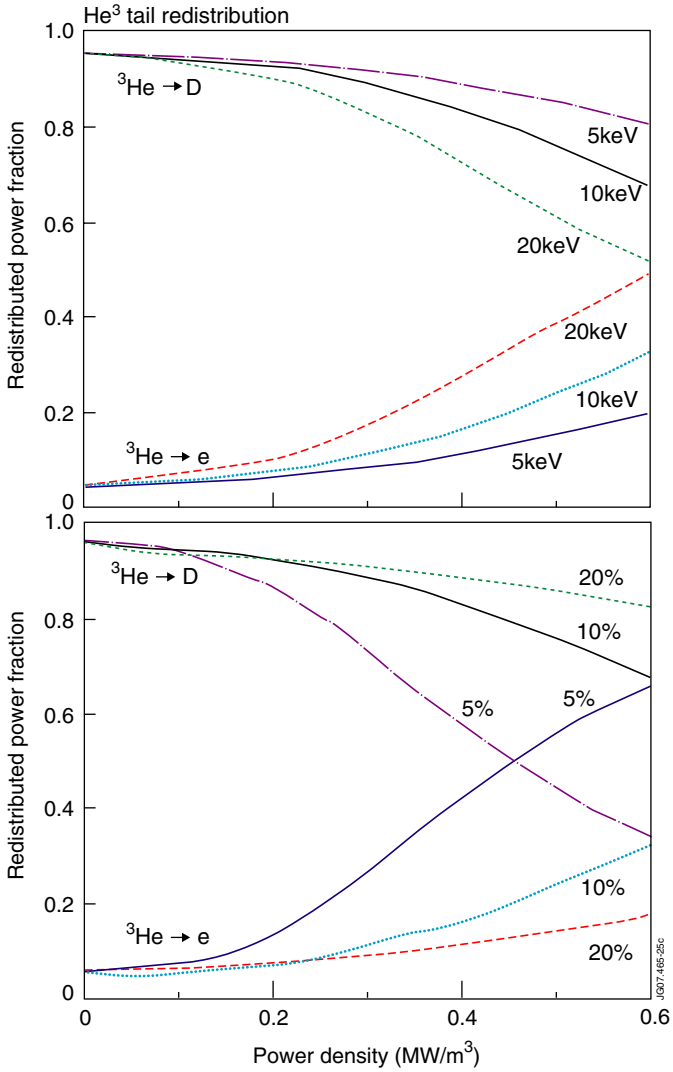

Figure 4. Collisional redistribution of the power absorbed by the ^{3}He minority to the electrons and bulk D ions as a function of the minority RF power density: (top) temperature scan, (bottom) ^{3}He concentration scan; other parameters as for the thermal plasma TOMCAT runs.

In the range of temperatures typical for JET operation, the total absorption is only a weak function of the species' temperature. Assuming that all particles share the same temperature and considering all parameters except the central temperature to be the same as above, it is found that all species together absorb 80–90% of the incoming power in a double transit over the plasma. At low temperatures minority heating is dominated by electron damping. Once the central temperature exceeds a certain value this heating scheme slowly becomes less efficient, and the ^{3}He minority becomes the main absorber of RF power. For $X[^3\mathrm{He}] = 10\%$ this happens at about 7 keV and the maximal fraction of the incoming power absorbed by the minority in a double transit is about 70%. The fact that this cross-over from electron to ion heating occurs has a practical consequence: the better the energy confinement in a plasma, the harder it is to reach the conversion regime.

When a fast minority is created by RF heating, the minority particles transfer the power they absorb from the waves to the bulk species by Coulomb collisions. For typical power densities that can be obtained in JET (roughly up to 0.3 MW m^{-3} for central heating and a fraction of that when off-axis heating is desired), the ^{3}He minority—opposite to the case of a H minority—transfers most of its power to the bulk ions; see figure 4 obtained using the simplified distribution function formalism proposed by Stix [12]. Only when very efficient core heating is applied and the ^{3}He concentration is relatively low does a significant fraction also go to the electrons by collisions. This characteristic is very useful when doing transport studies as it allows one to keep the ion and electron heat input channels separated.

2.2. RF heated D beam modeling

The TOMCAT code lacks a number of ingredients to make its predictions fully credible: As it is a 1D code, it neglects 2D-diffraction effects. Also it does not enable one to assess the role played by the poloidal magnetic field. The former limitation is commonly considered to be acceptable when modeling efficient heating schemes in large machines, while the second is not overly important when the fast wave is the dominant wave branch. In spite of its drawbacks, the TOMCAT code thus still gives a good qualitative impression of how RF heating in a big tokamak works. But most importantly, however, TOMCAT assumes that all plasma constituents are in thermodynamical equilibrium. When modeling RF *heating* of tokamak plasmas, this assumption is questionable at best. This section is devoted to the description of an important effect that is totally missed by TOMCAT (and, more generally, by any wave code built on the assumption that the distribution functions of all the plasma constituents are Maxwellians): the shifting of the position where the dominant absorption occurs away from the cold cyclotron resonance location.

D beam injection was routinely used to fuel and heat the (^{3}He)–D plasmas discussed in this paper. JET is equipped with two neutral beam injection banks, each having a 'normal' and a 'tangential' beam box. One beam box (in octant 8) has eight 130 kV/58 A tetrodes and can launch up to 6.4 MW tangential and 6.4 MW normal to the magnetic field. The other beam box, situated in octant 4, has four 80 kV/58 A normal injection modules totalling 6.6 MW as well as two 80 kV/54 A, a 130 kV/58 A and a 140 kV/30 A tangential injector delivering 2 times 1.6 MW, 1 MW and 0.6 MW, respectively. From the tangency radius $R = 1.85$ m for the tangential and $R = 1.31$ m for the normal bank, one can compute the local pitch angle of the ions upon ionization on each radial location. Although the cold deuterium cyclotron layer was far off-axis for the ^{3}He experiments, making bulk D heating very inefficient, the beam particles are nevertheless still sensitive to the RF electric field. Figure 5 gives an impression of what the energy of a mixed normal/tangential and 80/130 keV D beam distribution looks like at a magnetic surface $\rho = 0.02$ m close to the magnetic axis (where most particles are passing), at $\rho = 0.5$ m and at a surface $\rho = 0.9$ m close to the edge (where a large subpopulation of trapped particles exists). The variable ρ labels the magnetic surfaces. It is half the width of the magnetic surface in the equatorial plane. The distribution was evaluated on a set of magnetic surfaces using the BATCH 2D bounce averaged Fokker–Planck code [13] and with an RF electric field provided by the CYRANO full-wave code [14] which solves the wave equation accounting for the actual tokamak geometry and retaining up to second order finite Larmor radius corrections. At this stage, it is only meant to give a qualitative picture of what the non-thermal D subpopulation looks like. Work is ongoing to model this beam subpopulation in more detail coupling the BATCH code with the CYRANO wave equation code which is now equipped to handle non-Maxwellian populations [15, 16]. Running the two codes in a coupled way (the wave code evaluating the RF dielectric tensor accounting for the local

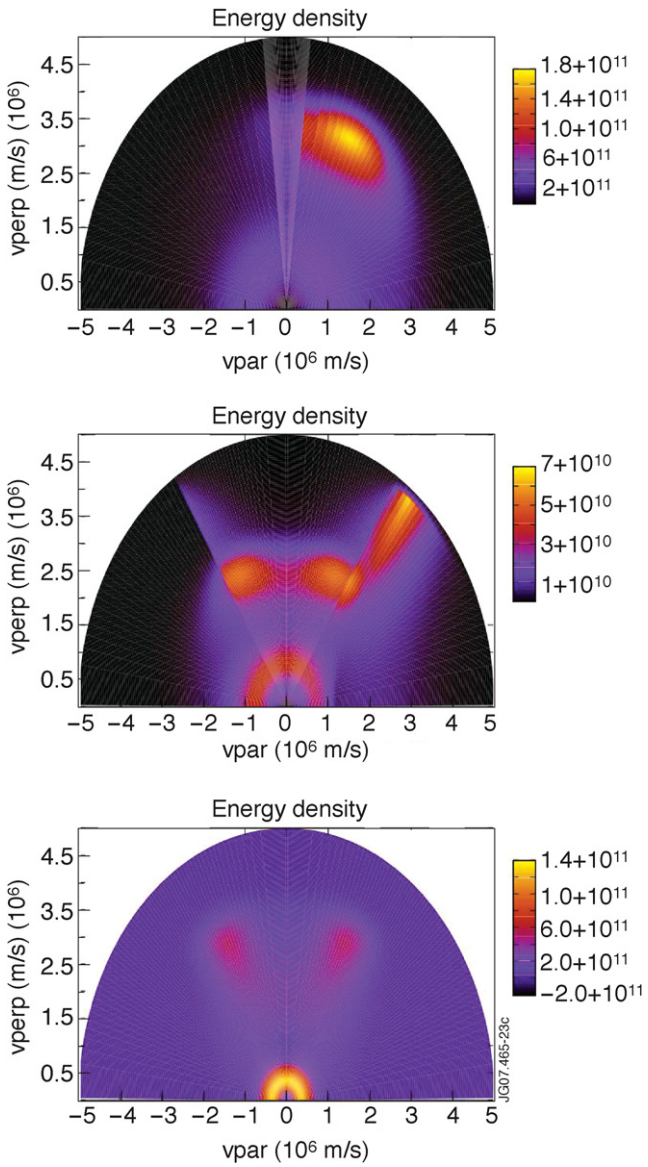

Figure 5. RF heated D beam energy density in a $(v_\perp, v_\parallel)$ diagram—the parameters chosen qualitatively represent those of the combined 80 + 130 keV and normal and tangential JET beams: (top) $\rho = 0.02$ m, (center) $\rho = 0.50$ m, (bottom) $\rho = 0.90$ m; ρ is the magnetic surface labeling parameter.

non-Maxwellian distribution function and the Fokker–Planck code evaluating its RF diffusion operator accounting for the field structure it imports from the wave code) yields a more detailed picture of how the beam and the RF heating synergistically interact [17]. A rough discussion of the CYRANO-BATCH coupling can be found in [16]. Other coupled wave+Fokker–Planck solvers have been proposed in the literature. The most sophisticated ones include finite banana width effects and RF induced radial diffusion, and/or solve the full integro-differential wave

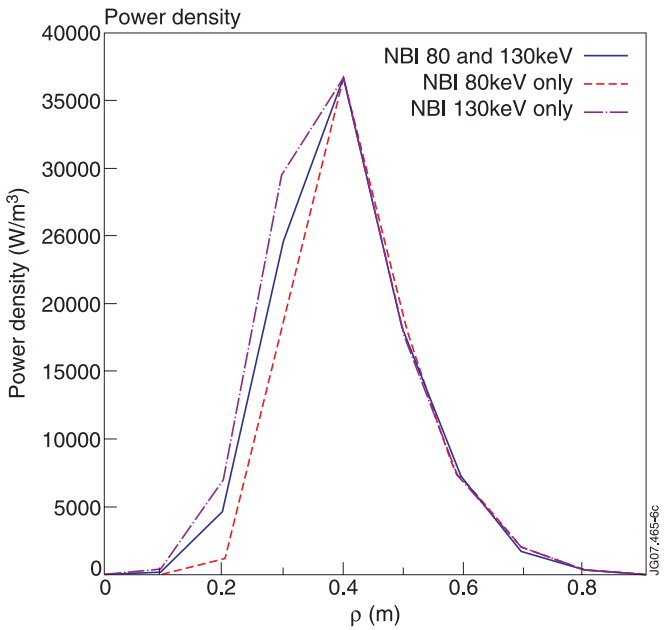

Figure 6. RF power absorption profile of JET D beam particles as a function of the flux surface labeling parameter ρ using the electric field provided by CYRANO for a 20% ^{3}He minority in a D plasma with $B_o = 3.4$ T and $f = 33$ MHz; the non-Doppler-shifted resonance is 0.64 m away from the magnetic axis while the beam source is assumed to peak at $\rho = 0.2$ m. The same analytical equilibrium as in TOMCAT was adopted in CYRANO and BATCH.

equation to retain all finite Larmor radius effects (see, e.g. [8, 18, 19]). Whereas BATCH solves the Fokker–Planck equation directly, various authors rely on Monte Carlo techniques to solve this equation by representing the studied population by a set of test particles (see, e.g. [19, 20]).

Figure 6 shows the power deposition profile obtained when solving the Fokker–Planck equation on a number of magnetic surfaces. Similar parameters as for the TOMCAT computation were taken and thus the cold (non-Doppler-shifted) D cyclotron resonance lies about 0.7 m away from the plasma core on the high field side. Note that the beam deposition is broad and spreads up to 0.1 m from the magnetic axis. This effect is enhanced when higher power densities are reached. The reason for this broad deposition is that the resonance of energetic particles is Doppler-shifted away from the cold resonance. For JET D beam particles with a birth energy of 130 keV, a purely tangential particle would have a Doppler shift of the order of 0.6 m for the dominant toroidal mode ($n = 27$) in the antenna spectrum when dipole phasing is used. Accounting for the actual pitch angle, this reduces to 0.45 m for the tangential and to 0.38 m for the normal 130 keV beam at JET. For the considered power density, a significant fraction of the beam particles has moderate energies when the steady state is reached between the RF power driving tails and the Coulomb collisions trying to reach thermal equiluibrium. Particles in the region around the cold resonance are RF heated, but the power deposition near the cold resonance is reduced because of the adverse polarization around $\omega \sim \Omega_D$ characteristic for majority heating schemes [21]. The radial distribution of the source is an important shaping factor for the RF power absorption profile of the beam distribution as well. To mimic the actual beam ionization profile infered from PENCIL simulations, a Gaussian $S = S_o \exp[-10.(\rho - 0.2)^2]$ centered around $\rho = 0.2$ m was taken as a beam

particle source here. A loss time $\tau = 0.3\,\mathrm{s}$ was chosen hence—as both the RF diffusion and Coulomb collisions are number conservative and assuming a steady state is reached—the local beam population density is $N = S\tau$ which maximally is about 10% of the total local plasma density.

Because the density and temperature and hence the collisionality depend on the magnetic surface labeling parameter ρ, because much more trapped orbits occur at the outer magnetic surfaces than at those close to the magnetic axis, and because each of the outer magnetic surfaces cuts the resonance layer while (for the adopted ^{3}He on-axis and thus D far-off-axis heating) the surfaces close to the core do not, the core and edge distributions are quite different, as can be seen in figure 5: whereas the distribution in the core is fairly isotropic while the energy density peaks at the beam source locations $(v_{\perp,\mathrm{in}}, v_{\parallel,\mathrm{in}})$, the distribution near the maximal deposition density and near the edge is showing the impact of RF heating at the tangent resonance and is more spread out in the perpendicular than in the parallel direction. Efficient heating, causing particles to diffuse towards higher energies, is observed both on the distribution (not depicted) and the energy density for $\rho = 0.5\,\mathrm{m}$. This spatial inhomogeneity necessitates having data from different diagnostics each independently focussing on different sub-fractions of the total configuration space to be able to find out in the experiment what the distribution function locally looks like along the path 'seen' by a diagnostic. Seemingly conflicting observations from different diagnostics may in reality just be highlighting specific aspects of the same particle population.

3. Determination of the experimental RF power deposition profile

As a periodic modulation of the RF power yields a periodic variation of the temperature, a frequently used method to get an idea of the experimental power deposition profile is to modulate the launched power level, commonly using a square wave modulation. Assuming transport as well as losses are absent—or (and physically more acceptable) happening on a time scale that is much longer than the chosen modulation period—the relation between the local energy $\epsilon = \frac{3}{2}NkT$ of the particles that absorb the incoming RF power, and the local wave power density transfered to these particles is simply $\partial\epsilon_\alpha/\partial t = P_\alpha$. A square wave modulation thus gives rise to a triangular wave form (i.e. a periodic linearly increasing and decreasing signal) for the energy. Studying the 'breaks' of the energy immediately yields an idea of where the wave power is experimentally absorbed. This elementary method for determining the experimental power deposition profile is often referred to as BIS or 'break-in-slope' analysis (for an in depth paper on this topic, consult e.g. [22]). Note that this method does not even require the power to be modulated periodically: a single power level jump is all that it needs.

The energy response to a given power level does not keep growing linearly with time, however. Various processes cause the energy to saturate such that—ideally—a steady state regime is reached. Without worrying about the physical interpretation of what brings about this saturation, the simplest ad hoc model to incorporate it consists of adding a loss term with a characteristic time τ to the source term in the simple evolution equation for ϵ: $\partial\epsilon_\alpha/\partial t = P_\alpha - \epsilon_\alpha/\tau_\alpha$. The exponential solution of this equation reduces to that for the linear response if the period of the modulation is much shorter than the characteristic time on which the 'slow' plasma variations occur. It is clear that the simple loss term is much too crude to shed light on the actual reason of why the plasma energy saturates. A large number of phenomena such as actual loss/gain processes (think e.g. of charge exchange which locally 'annihilates' or 'creates' heat stored by some category of charged particles) but also transport (importing heat from or evacuating it away to neighboring magnetic surfaces). Also

linearization of the equations results in terms that are proportional to the perturbed energy and thus can formally be written as loss/gain terms.

The parameters in the linear as well as the exponential fit are obtained performing a minimization of the square of the 'distance' D, $D^2 = \sum_{\text{data}}(\epsilon_{\text{exp}} - \epsilon_{\text{fit}})^2$, between the experimental data and the proposed fit. Because the energy response does not necessarily coincide with the instants at which the RF power changes, the time of the breaks in the slopes is used as one of the parameters in the minimization. For some of the parameters the regression can be done analytically, while for others a numerical minimization procedure is required.

Fast Fourier transformation is a third method standardly used to study the response of a particle population to the modulation of the RF power. This method is often preferred when transport is studied (see [23] and the references therein, and see the subsection on transport).

On JET the high resolution 96-channel electron cyclotron emission diagnostic provides a detailed picture of the electron temperature [24], while charge exchange recombination spectroscopy (CXRS) yields the ion temperature with somewhat less resolution [25]. Figure 7 depicts the temperatures as well as the various applied auxiliary heating powers and the Ohmic power for ^{3}He minority heating shot number 69387 X[^{3}He] = 6%. As the dynamics of both ions and electrons are of interest for the study of the fate of the RF power and since the energy confinement time as well as the slowing down time are of the order of a few hundred ms, the RF power is modulated at a 6 Hz modulation frequency. Strictly this frequency is more suitable for ion than for electron analysis (for electron analysis a modulation frequency bigger than 15 Hz is usually preferred; electron transport was studied extensively in earlier campaigns [26, 23]). Both the ion and the electron temperature signals exhibit a clear response to the RF modulation. For the chosen frequency and magnetic field, $f = 33$ MHz and $B_{\text{o}} = 3.35$ T, the ^{3}He cyclotron layer is more or less central ($R = 3.07$ m).

Although the density response to the RF power should strictly be accounted for as well, it is assumed here that it is negligible compared with that of the temperature. Local density measurements with a high temporal resolution are not yet available at JET. The density profile is provided with a 4 Hz temporal resolution on about 50 spatial channels by the Thomson scattering LIDAR diagnostic [27]. High temporal resolution density information is only available via the KG1 interferometer but this diagnostic gives line integrated rather than local information. Density perturbations are observed to be important when the RF heating efficiency is low and large electric fields in the edge non-resonantly accelerate particles, a subfraction of which hits the wall and enhances recycling, leading e.g. to 'RF cooling' of the edge at the switch-on of the RF generators (see, e.g. [28]). For the ^{3}He experiments, the absorptivity was high enough to avoid extreme outgassing, allowing to safely omit the density response to the modulation when analyzing the data.

Figure 8 depicts one of the central electron temperature channels in a narrow time window suitable for FFT/BIS analysis. The top figure provides the raw T_{e} signal, as well as the signal smoothed over a full period $\langle T_{\text{e}}\rangle$ to remove slow time variation, and the signal smoothed over 20% of a period $[T_{\text{e}}]$ to reduce the high frequency noise on the signal. The slow variation is discarded by subtracting the $\langle T_{\text{e}}\rangle$ signal to retain only the evolution driven by the modulation (middle figure). The analysis is then performed on $[T_{\text{e}} - \langle T_{\text{e}}\rangle]$. Together with $[T_{\text{e}} - \langle T_{\text{e}}\rangle]$ the linear and exponential fits obtained after minimization are shown in the bottom figure. The fundamental Fourier amplitude is shown as well. For this shot all methods give similar results. The corresponding power deposition profiles are plotted in figure 9. Both the ion and electron deposition profiles peak in the plasma core for minority heating shot 69387. The integrated powers are plotted as well. In total, the electrons absorb ≈30% of the externally launched RF power and the ions about 60%. The fact that only 10% of the power seems to be unaccounted for is somewhat illusory: in the outer

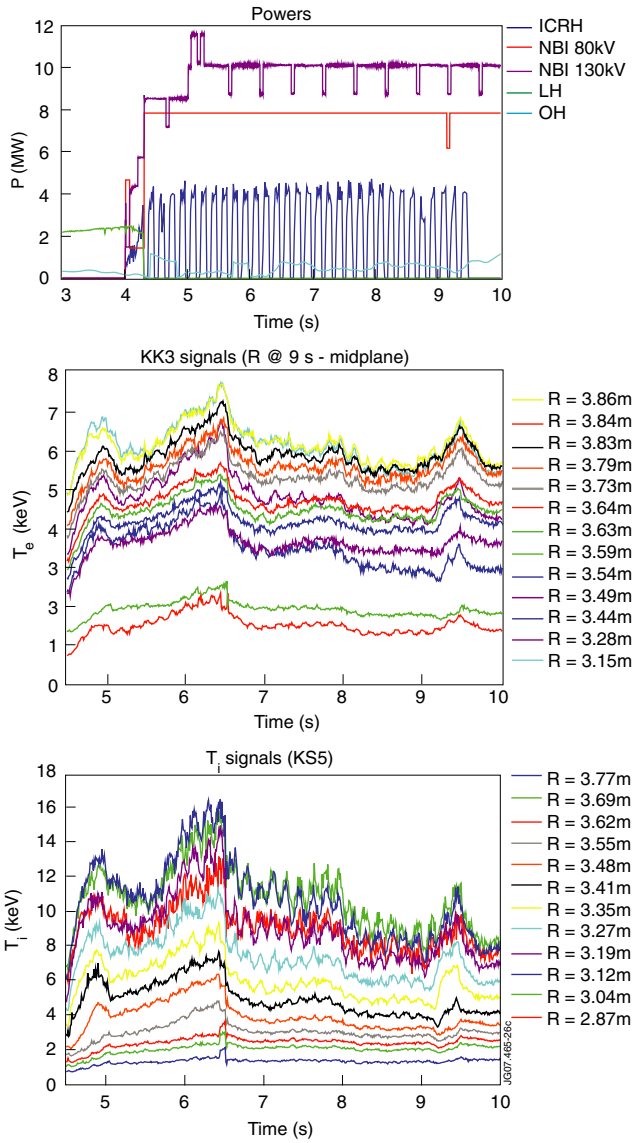

Figure 7. On-axis RF heating (shot 69387) shown as a function of time: (top) various power levels, including the RF power P_{ICRH} modulated at a frequency of 6 Hz, (middle) electron temperature T_{e} and (bottom) ion temperature T_{i} as a function of time. The charge exchange periscope from which T_{i} was inferred was tuned to ^{3}He.

layers where the power density is low, the volume between two magnetic surfaces is large. Hence small errors on the local power density estimate yield substantial errors on the power integral.

Although RF power modulation was initially used to study the experimental heat deposition profile and to check which fraction of the externally launched power was actually found back in the plasma, it was soon realized that the spreading of the locally deposited energy through heat diffusion—an at first sight undesirable effect as it deforms the actual deposition

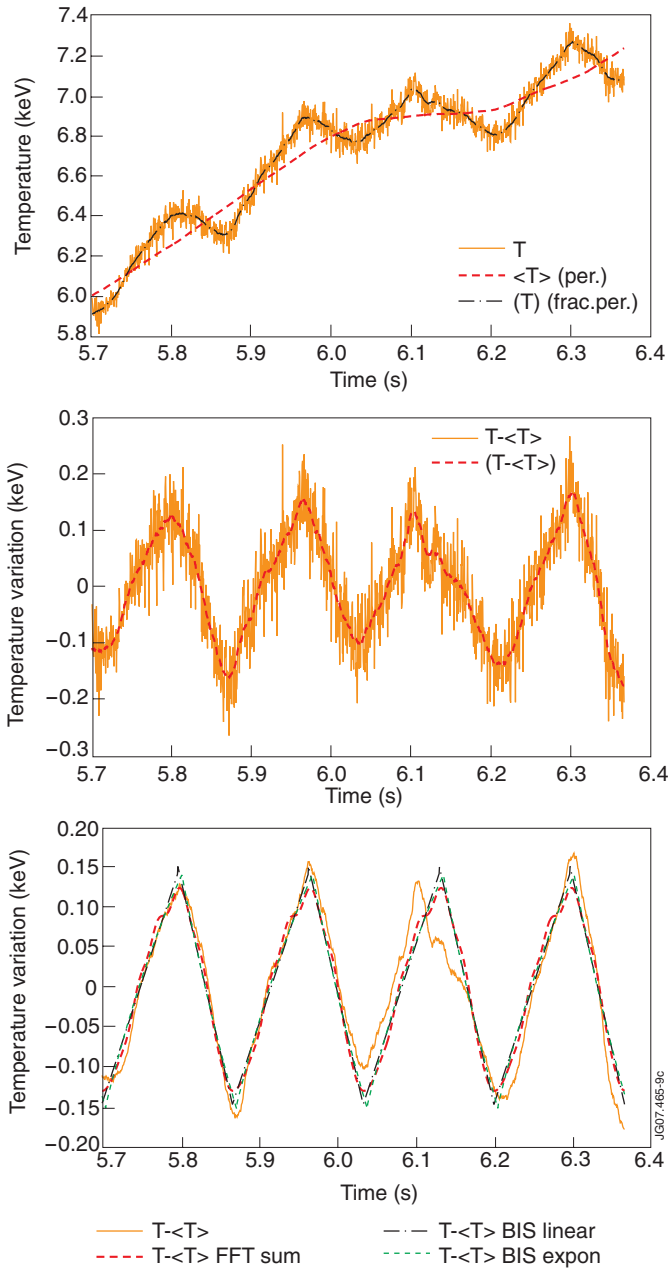

Figure 8. Electron temperature response at $R \sim 3.2$ m to RF power modulation for shot 69387 during the ITB shown as a function of time: (top) raw ECE data T_e as well as data smoothed over a full modulation period $\langle T_e \rangle$ to remove slow time variation and $[T_e]$ over a fraction (typically 20% of the period) to remove the most rapid variation but retaining modulation-related trends, (middle) $T_e - \langle T_e \rangle$ and $[T_e - \langle T_e \rangle]$ (input for further data analysis), (bottom) FFT fit, linear fit and exponential fit of $[T_e - \langle T_e \rangle]$.

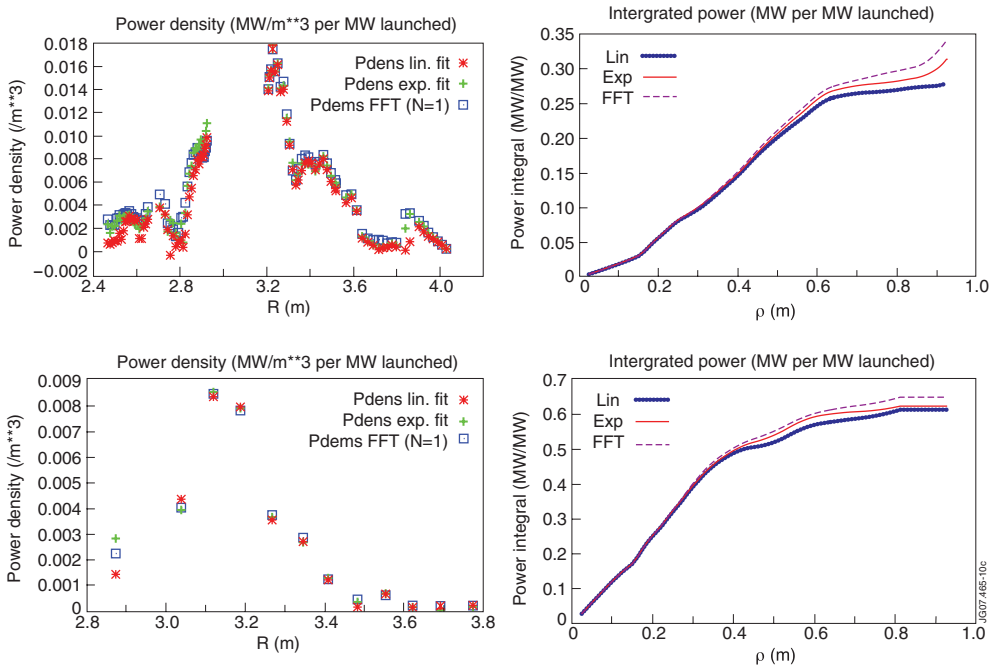

Figure 9. Power density as a function of major radius: on-axis RF heating (shot 69387) with main parameters $B_o = 3.35\,\mathrm{T}$, $f = 33\,\mathrm{MHz}$ (dipole phasing), $T_{o,e} = 7$–$8\,\mathrm{keV}$, $T_{o,i} = 14\,\mathrm{keV}$, $N_{o,e} = 4 \times 10^{19}\,\mathrm{m}^{-3}$: (top left) electron power density, (top right) integrated electron power absorption, (bottom left) ion power density, (bottom right) integrated ion power absorption.

profile—can be used to diagnose the transport and to find its diffusion characteristics by solving the heat and particle transport equations adjusting parameters in the model attempting to mimic experimental findings. These transport equations often are equations of the Braginskii type but with extra freedom left by adding some empirical expression for the turbulence (e.g. ITG or ETG) driven diffusion. Making guesses of the local diffusivity and modifying the model's free parameters until a reasonable agreement between the experimental and theoretically predicted temperature response is obtained (see, e.g. [23]) allows one to separate the response to heating from that due to heat wave propagation. To date, no first principle theoretical models exist that satisfactorily describe the actual transport of charged particles and heat in magnetically confined hot plasmas. Lacking such models, empirical or semi-empirical ones are adopted to shed light on the nature of transport and to help theory to get a firmer grip on which ingredients need to be included in a realistic model. In view of the experimental observation that some tokamaks exhibit 'stiff' transport, critical gradient models have been proposed and successfully used. Such models start from the assumption that turbulence lifts transport well above the neoclassical level once the temperature gradient exceeds a threshold. This kind of model was equally adopted to study the transport in JET [29] (see further).

4. Real time control of the ^{3}He concentration

To ensure that the localized heat source does not move as a function of time, mode conversion heating studies rely on being able to maintain the ^{3}He concentration as constant as possible. Although the position of the dominant minority heating does not sensitively depend on the value of the minority concentration (the cold resonance does not depend on it at all), keeping

$X[^3\mathrm{He}]$ fixed facilitates the interpretation of the experimental findings for minority heating as well since the absorption efficiency critically depends on $X[^3\mathrm{He}]$. Ensuring a constant $X[^3\mathrm{He}]$ has been done by constructing a real time controlled feedback loop which drives the ^{3}He gas injection modules whenever the desired concentration falls under a predetermined value [30]. Such a feedback loop requires having an approximate but sufficiently realistic expression for the ^{3}He concentration which can be evaluated in real time during the discharge. Relying on the local charge neutrality and on the definition of Z_{eff}, Mantsinen worked out a formula to guess the ^{3}He concentration assuming the only plasma impurity is carbon. This indeed being the case for scenarios not interacting violently with the wall and in which no impurities are purposely injected, this expression was successfully applied when studying mode conversion in L-mode plasmas [26]. For more extreme circumstances—as e.g. H-mode or ITB plasmas—the formula needed to be generalized to include the effect of other impurities besides C present in the plasma. Adopting the same computational strategy, the generalized result is

$$X[^3\mathrm{He}] = \frac{Z_{\mathrm{eff}} - \gamma_{\mathrm{imp}}}{(1-\gamma_{\mathrm{imp}})\dfrac{X[\mathrm{D}]}{X[^3\mathrm{He}]} + 2(2-\gamma_{\mathrm{imp}})}$$

in which $\gamma_{\mathrm{imp}} = \beta/\alpha$, where $\alpha = 6 + \sum_i Z_i X[\mathrm{Imp}_i]/X[C]$ and $\beta = 36 + \sum_i Z_i^2 X[\mathrm{Imp}_i]/X[C]$, and where the sum is on all impurities except carbon. The key philosophy adopted is that the intensity of a spectral line (e.g. the intensity of the photon flux from the Balmer α line emitted by D) is proportional to the density of the emitting particles and thus—provided the light intensity is only a weak function of other parameters—the relative densities $X[\mathrm{D}]/X[^3\mathrm{He}]$ and $X[\mathrm{Imp}_i]/X[\mathrm{C}]$ in the above formula can be inferred from relative measured light intensities provided the proper proportionality factor is known. Although this yields a somewhat crude guess of the concentrations it is sufficiently accurate to be used in a real time control loop during the experiments. Note that not only $X[^3\mathrm{He}]$ but also the concentration of all other ion species can be evaluated by inferring $X[\mathrm{D}]$ from $X[^3\mathrm{He}]$ and $X[\mathrm{D}]/X[^3\mathrm{He}]$, and $X[\mathrm{Imp}_i]$ from $X[\mathrm{C}]$ and $X[\mathrm{Imp}_i]/X[\mathrm{C}]$ after solving the charge neutrality expression and the definition equation of Z_{eff} for α and β and deducing $X[\mathrm{C}]$ from $X[^3\mathrm{He}]$ and $X[\mathrm{C}]/X[^3\mathrm{He}]$. When the density profile changes considerably during the discharge, a simple peaking factor (central over edge/pedestal density at any given time divided by the value of this quantity at a reference time) is further applied to the above formula in an ad hoc way. A more accurate evaluation of the concentration is obtained from post-processing charge exchange measurements [25]. These data not only yield a typical concentration as a function of time, which is all the simple formula does, but equally provides the $X[^3\mathrm{He}]$ profile evolution. Figure 10 depicts an example of how the simplified formula is used to steer the real time control of the ^{3}He concentration. Almost surprisingly in view of its simplicity (the relation between a particle density and the intensity of the emitted light is actually a function of various parameters that change both in time and in space), the real time control formula commonly catches the proper tendency of the actual concentration and is usually well within 50% of the requested value in the auxiliary heated flat top phase of the experiments.

5. RF heating, fast particle populations and MHD activity

The observation of the link between fast particles and MHD activity dates from decades ago: soon after Mc Guire *et al* reported on the experimental observation of fishbones on PDX [31] in 1983, White *et al* identified a possible mode-particle pumping loss mechanism [32]. This was in turn followed by a theoretical explanation of the internal kink excitation [33]. More recently, Sharapov reported on TAE modes being excited by RF waves in JET [34].

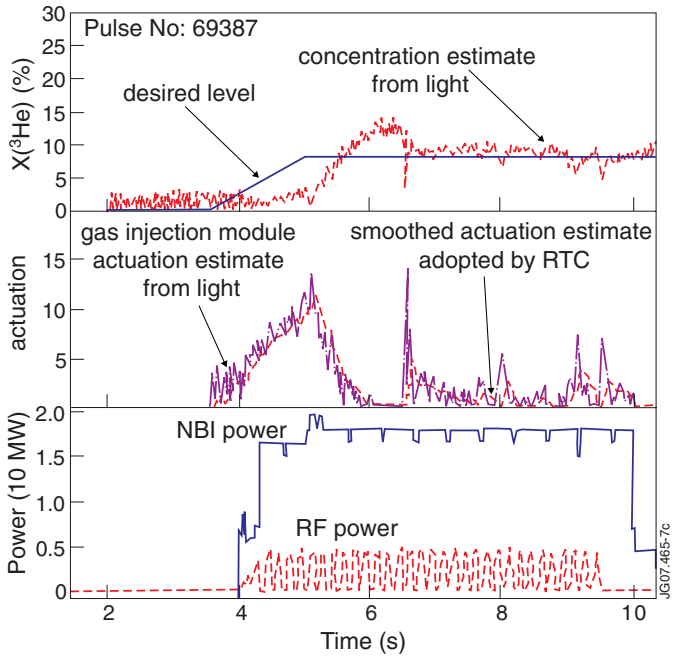

Figure 10. Example of real time control of the ^{3}He concentration (based on the photon fluxes—e.g. the intensity of the D_α line—emitted by various ion species) for discharge 69387: desired concentration and actual concentration as estimated using the simplified formula adopted by the real time controller (top), raw gas injection module valve actuation required to ensure the desired concentration is maintained (inferred from the simple formula) as well as smoothed actuation actually used (middle), and NBI and RF power level (bottom). Note that it takes some time for the real time controller to match the desired concentration: when the auxiliary power is switched on the whole plasma is undergoing a slow evolution towards a steady state regime and freezing the concentration is nontrivial.

Without ^{3}He injection, the only ^{3}He coming into the plasma is the tiny fraction residing in and evacuated from the machine wall from recent earlier ^{3}He experiments. Experiments aiming at exciting MHD modes driven by RF heated fast particle populations allowed fishbones, toroidal Alfvén eigenmodes and Alfvén cascades to be observed when $X[^3\mathrm{He}]$ was 1% or below [35].

As no particular MHD activity was triggered in its absence, RF heating played an essential role in these experiments. A careful study of the gamma ray spectrum allows one to get insight in the fusion reactions that occurred. Evidence of various types of fast orbits/ions was found. The presence of gamma rays [36] with energies in the range ≈10–18 MeV proves that the reaction $\mathrm{D} + {}^3\mathrm{He} \rightarrow {}^5\mathrm{Li} + \gamma\,(16.4\,\mathrm{MeV})$ is taking place. The latter requires the presence of sufficiently energetic fuel particles and thus demonstrates that a sub-population of the ^{3}He is being heated efficiently by the RF waves. A first assessment suggests that ^{3}He tails of maximally 500 keV were created. High-energy protons are required to trigger the equally observed $^{12}\mathrm{C}(\mathrm{p}, \mathrm{p}'\gamma)^{12}\mathrm{C}$ threshold reaction producing 4.4 MeV γ rays. As the RF generator frequency was tuned to heat ^{3}He and not H, these energetic protons likely arise from the $D + {}^3\mathrm{He} \rightarrow {}^4\mathrm{He}(3.6\,\mathrm{MeV}) + \mathrm{p}(14.7\,\mathrm{MeV})$ reaction.

Significantly reducing the RF power during intervals of a few hundred milliseconds allowed to clearly identify the effect of the RF heating on the MHD activity: modes disappeared

or became much weaker when the RF heating level was reduced, in good agreement with expectation from theory predicting that such modes rely on fast particle 'current sources' for their excitation [31, 37, 38]. A scintillator probe allows one to study fast ion losses. Fusion-produced 15 MeV protons—with Larmor radii of 13 cm—constitute the dominant loss. Both the number and the energy of lost fast ions [39] correlated with the RF power; the effect of the slowing down of the fast particles (fusion-created protons) can clearly be observed on the lost ion time traces.

The experiments performed at very low $X[^3\mathrm{He}]$ aimed at studying confinement and redistribution of fast ions and focused on determining the impact of fast particles on MHD activity. Tornado modes [40], held responsible for expelling fast ions from inside the $q = 1$ radius and for triggering monster sawtooth crashes, were aimed for but were not observed. On the other hand, $n = 1$ fishbones were excited: they preceded every sawtooth crash (n is the toroidal mode number). Both fishbones and tornado modes are depending on energetic particles for their excitation, and both types of mode affect the fast ion population inside the $q = 1$ radius. Thanks to the fast ^{3}He particles created by RF heating, the sawtooth period could be increased and monster sawteeth were observed.

Since charged particle orbits are highly sensitive to the magnetic field topology and sawteeth change this topology on a very rapid time scale, one can anticipate that the orbits and thus the fusion yield undergo equally rapid changes when sawtooth crashes occur. During the experiments with small RF heated ^{3}He concentrations, fishbone activity (itself characterized by a frequency of 5–20 kHz) was observed to re-occur periodically with a frequency of ∼150 Hz. This fishbone activity was interrupted regularly because sawtooth crashes were occurring on a much longer time scale (∼4 Hz). Figure 11 shows the effect of the redistribution of the ^{3}He ions, the top figures showing the tomographically reconstructed gamma ray emissivity for gamma's with energies exceeding 2.2 MeV and averaged over a 150 ms interval. Since the reactivity giving rise to the gamma rays is proportional to the density of the fast (^{3}He) particle population, the emissivity profile sheds light on the spatial distribution of the RF heated ions. A brighter color represents a higher count rate. The left figure is the profile before and the right figure shows the emissivity just after a sawtooth crash. The auxiliary heating power (NBI + ICRH) is roughly constant in the time interval considered. The bottom figure shows the frequency spectrum of the modes as a function of time.

JET is equipped with a scintillator probe designed to detect very fast (fusion born) ion losses [39]. Both the protons and the α particles born out of the ^{3}He + D reaction have broad energy distributions at birth. Prompt proton losses are however far outside the scintillator probe area and cannot be observed. Therefore the observed components from the ^{3}He + D reaction are fast α particles. These losses are clearly correlated—not only with the RF power as above mentioned—but equally with the sawtooth crashes.

In case RF heating creates fast particle populations, so-called Alfvén 'cascades' are triggered when the minimum value of the safety factor $q_{\min}$ is rational, each mode satisfying $nq_{\min} = m$; (m is the poloidal mode number). Because the time derivative of the Alfvén frequency $\omega_{\mathrm{AC}} = V_{\mathrm{A}} k_{\|}$—with V_{A} the Alfvén velocity and $k_{\|} \approx (n - m/q_{\min})/R_{\mathrm{o}}$ the parallel wave number—changes as the time derivative of $m/q_{\min}$, the cascades' frequency increases as $q_{\min}$ decreases. Figure 12 shows the Alfvén cascades observed in discharge 69445, having a ^{3}He concentration of less than 1% heated centrally using RF heating with $f = 33$ MHz while $B_{\mathrm{o}} = 3.25$ T; $+\pi/2$ phasing was preferred to profit from the associated radially inward RF induced fast particle pinch [41]. When $q_{\min}$ is an integer, a 'grand' cascade is formed: various Alfvén modes share the same frequency at the time of their birth and are then frequency-separated at a rate proportional to the relative poloidal mode number ($\delta\omega_{\mathrm{AC}} \propto \delta(m/q_{\min})$). Cascades are excellent diagnostics for internal transport barriers

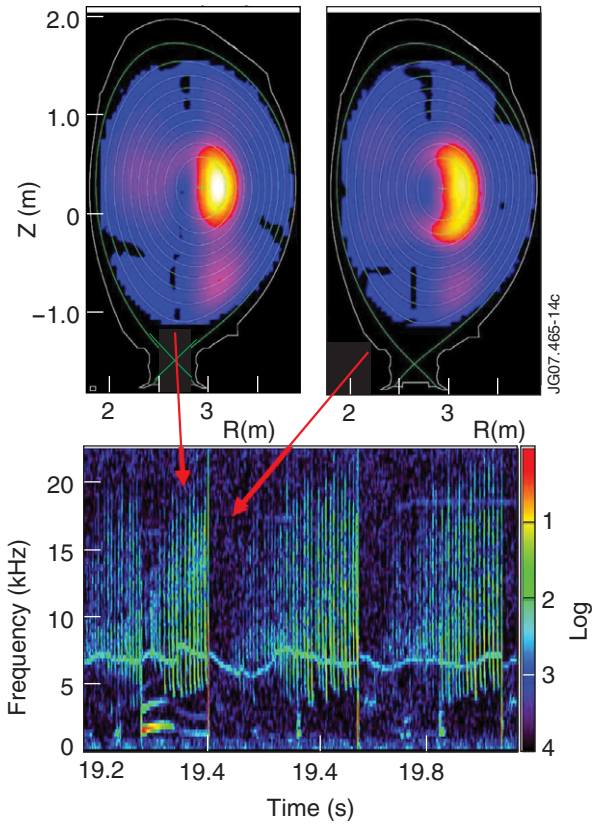

Figure 11. Tomographical reconstruction of the gamma ray emissivity for gamma's with energies exceeding 2.2 MeV. The top plots represent the emissivity averaged over 150 ms just prior to (left) and just after (right) a sawtooth crash. The bottom plot is the frequency spectrum of the plasma's magnetic activity as a function of time, showing the presence of fishbone activity prior to sawtooth crashes.

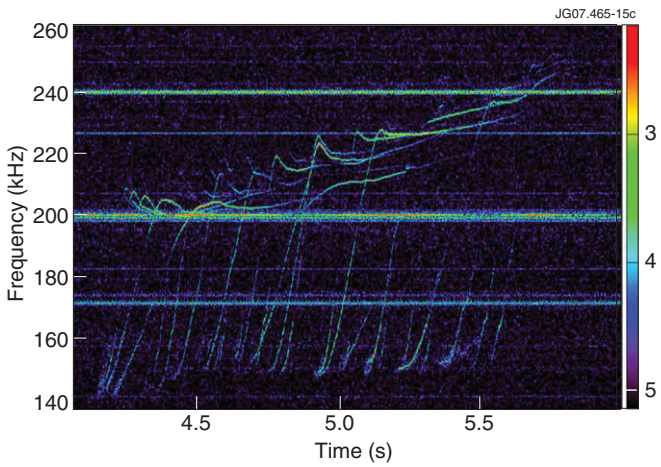

Figure 12. Magnetic activity frequency spectrum as a function of time showing Alfven cascades in shot number 69445.

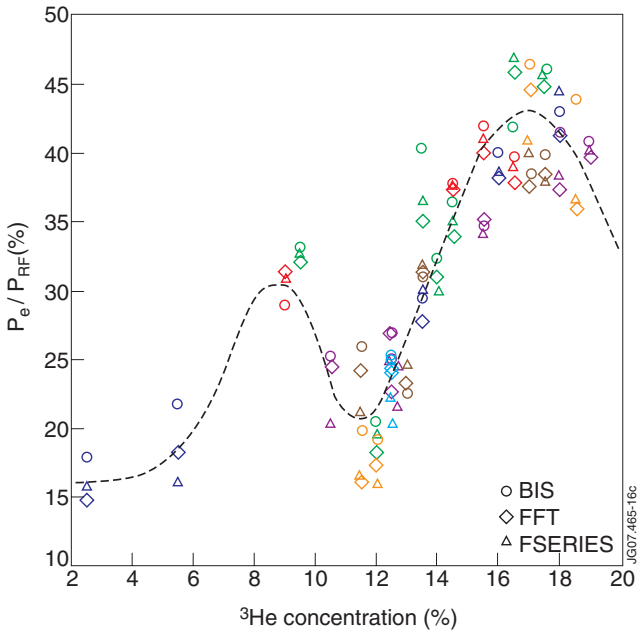

Figure 13. Power fraction directly or indirectly absorbed by the electrons for shots 66413–66437 as a function of $X[^3\text{He}]$. Various analysis techniques were adopted. Circles, diamonds and triangles denote results obtained using break-in-slope, fast Fourier transform and truncated Fourier series analysis, respectively. Optimal electron heating occurs at $X[^3\text{He}] \approx 17$–19%, a secondary maximum is found at $X[^3\text{He}] \approx 8$–9% while the absorption is poorest at $X[^3\text{He}] \approx 11$–13% and at low concentration.

(ITBs) [42]: there is a one-to-one relation between the time ITBs are formed and the time cascades are appearing. Of course, as cascades necessitate the presence of a sufficiently high concentration of sufficiently fast particles, they only exist when auxiliary heating is capable of creating a fast sub-population to excite them. Hence this accurate ITB 'detection' tool is not always available. RF heating is commonly used to create the instrumental fast population. As already mentioned, this is easier in a H minority than in a ^{3}He minority plasma, except when $X[^3\text{He}]$ is very small.

6. The Fuchs *et al* standing wave effect

Theoretical wave propagation and damping modeling (see the section on the modeling of RF heating in ^{3}He plasmas) indicates that the absorption efficiency in (^{3}He)–D plasmas depends strongly on various parameters. The standing wave effect identified by Fuchs *et al* [11] and arising because of the constructive/destructive interference of fast waves traveling to and from the high field side fast wave cutoff in scenarios with a fairly transparent mode conversion layer (such as is the case for a (^{3}He)–D mixture) is expected to be most clearly observable when scanning the electron density (which changes the fast wave wavelength), the magnetic field (which displaces the mode conversion layer) or the minority concentration (which equally changes the mode conversion layer position).

A minority concentration scan was performed in shots 66413–66437 and the RF power was modulated to infer the power deposition profile from break-in-slope (BIS) or fast Fourier

transform (FFT) analysis. Figure 13 shows the fraction of the power absorbed by the electrons integrated up to $\rho = 0.8$ m. There is a pronounced maximum of the absorptivity at $X[^3\mathrm{He}] \sim 18\%$, and a secondary maximum at $X[^3\mathrm{He}] \sim 8\%$. From the analysis of the phases of the examined heat fronts one can infer that the absolute maximum (at 18%) is mainly due to direct absorption of RF power whereas the secondary maximum (at 8%) is the result of mixed direct and indirect RF heating. The former is associated with the direct absorption by the electrons of both wave power carried by the short wavelength branches—excited by the fast wave at the ion–ion hybrid layer—and wave power absorbed from the fast wave itself. The other maximum is mainly associated with mixed minority and electron absorption, a fraction of the minority power being channeled to the electrons via Coulomb collisions for sufficiently central minority heating.

Whereas this data is qualitatively consistent with the theoretical prediction, the curve is not fully populated in the minority heating nor in the deep mode conversion regime. Also, the concentration at which the bigger maximum is reached is not fully consistent with the theoretical calculation shown in figure 2. A number of possible causes could explain this discrepancy: The predictions were obtained with a 1D wave model whereas one can expect the actual 2D or 3D wave pattern forming in the tokamak to have an impact on the result: there is an intimate relation between standing waves and the geometry in which they occur. The computations were done for a single (albeit the dominant) toroidal mode number of the antenna. Here again the weight of the tokamak geometry is not properly accounted for. Finally, as the fast wave's wavelength is a function of the density the experimental density profile should be used in the computations. The completion of the experimental curve as well as the more detailed modeling relying on more appropriate tools is outside the scope of the present summary but is planned to be addressed in the future.

7. RF heated D beam ions in mode conversion heating

Since ^{3}He is 3 times more massive than H, minority heating of ^{3}He in (^{3}He)–D plasmas produces less energetic tails than those observed in (H)–D. Since these moderately energetic ^{3}He tails predominantly slow down on ions, this guarantees a clear separation of the ion and electron heat channels. For that reason ^{3}He is often preferred as a minority gas for performing transport studies in which one tries to affect only one of the channels, preferring minority ion or mode conversion heating to affect the ion or the electron channel, respectively. For scenario's relying on neutral beam injection, however, this clean separation of ion and electron dynamics is blurred since a supplementary phenomenon comes into play: it was experimentally observed that in NBI D fueled and RF heated (^{3}He)–D plasmas intended to be in the mode conversion regime, not only the electrons are heated but also fast ion tails are formed. The first evidence of this effect was discussed by Mantsinen [26] already in 2004. It was clearly demonstrated that for otherwise similar working conditions in the mode conversion regime in a ^{3}He–D plasma, the phasing of the antenna allowed to change the neutron rate by up to a factor of 4. Since the ion temperature was not significantly different in the various shots, one had to conclude the observed effect was not due to a change in the bulk ion temperature. A tentative explanation was that the fast D beam particles—with energies exceeding their birth energy—were in some or other way responsible. Gamma ray spectroscopy substantiated this argument, demonstrating that fast D ions were indeed present: a clear line of gamma rays of 3.1 MeV arising from the $^{12}\mathrm{C(d, p}\gamma)^{13}\mathrm{C}$ reaction was identified.

One of the key advantages of gamma ray spectroscopy is that the peaks at well defined energies unambiguously prove that well defined reactions are taking place, thus guaranteeing

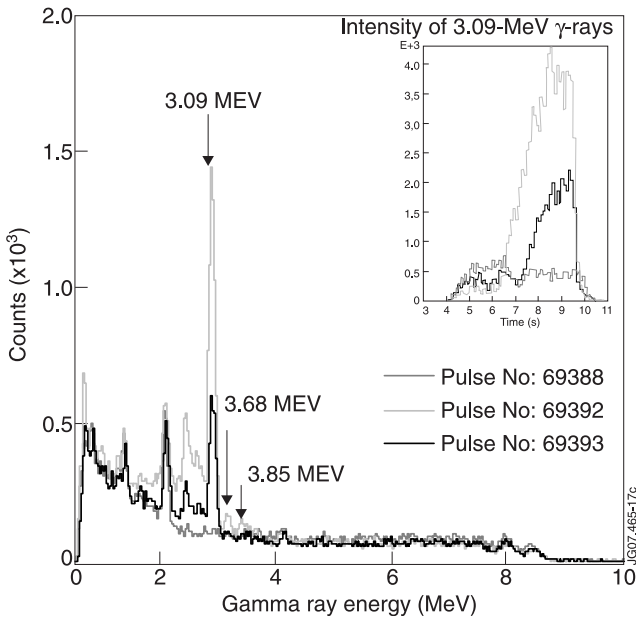

Figure 14. Gamma ray spectra recorded from 7.5 to 9.5 s in discharges 69388, 69392 and 69393. The temporal evolution of the rate of the 3.09 MeV gamma-line resulting from reaction ^{12}C(D, pγ)^{13}C marked in the spectra is shown in the inset; the same gray coding is used in both figures.

that the basic reactants for a given reaction are present in the plasma. Once the presence of a fast subpopulation of reactants has been demonstrated, other diagnostics provide supplementary information e.g. on the distribution of the particles causing the observed reaction. In these earlier experiments, a high-energy neutral particle analyzer showed that the D distribution function exhibited a tail reaching into the megaelectronvolt range.

The more recent experiments further confirmed the creation of this D tail, and offered supplementary results on the fast D population. Evidence of the D-ions tail was obtained from the gamma ray spectra, as can be seen in figure 14. In the later stage of shots 69393 and 69392—both with X[^{3}He] $\approx$ 18%—a clear 3.09 MeV peak is observed in the gamma ray spectrum. As already explained at the outset of this section, this peak arises from a reaction involving C^{12} and D, and yields an estimate for the D-tail temperature in the early, respectively, late phase of shot 69392 of below 150 and larger than 300 keV. The same peak is smaller but still very pronounced for shot 69393 while it is totally absent in shot 69388 (with X[^{3}He] $\approx$ 8%). For the minority heating pulse—69388—gamma ray and NPA data allow one to state that the ^{3}He (as opposed to the D) tail temperature is of the order of 100 keV. Furthermore, neutron time-of-flight spectra from the TOFOR neutron spectrometer (time of flight optimized for high rate) [43] are presented in figure 15 for JET pulses 69388 (top), 69392 (middle) and 69393 (bottom) [44], with the corresponding RF and NBI power levels shown in figure 16. The neutron time-of-flight spectra are dominated by a peak around 65 ns, which primarily corresponds to neutrons of 2.45 MeV from D + D $\rightarrow^3$ He + n fusion reactions involving the NBI ions and the thermal bulk plasma; in case there would be no thermal broadening whatsoever, the 2.45 MeV reaction's signature would be a sharp peak localized at 65 ns. Because the ^{3}He + D reaction does not produce neutrons and because knock-on effects are of much reduced intensity compared with the observed phenomena, TOFOR does not

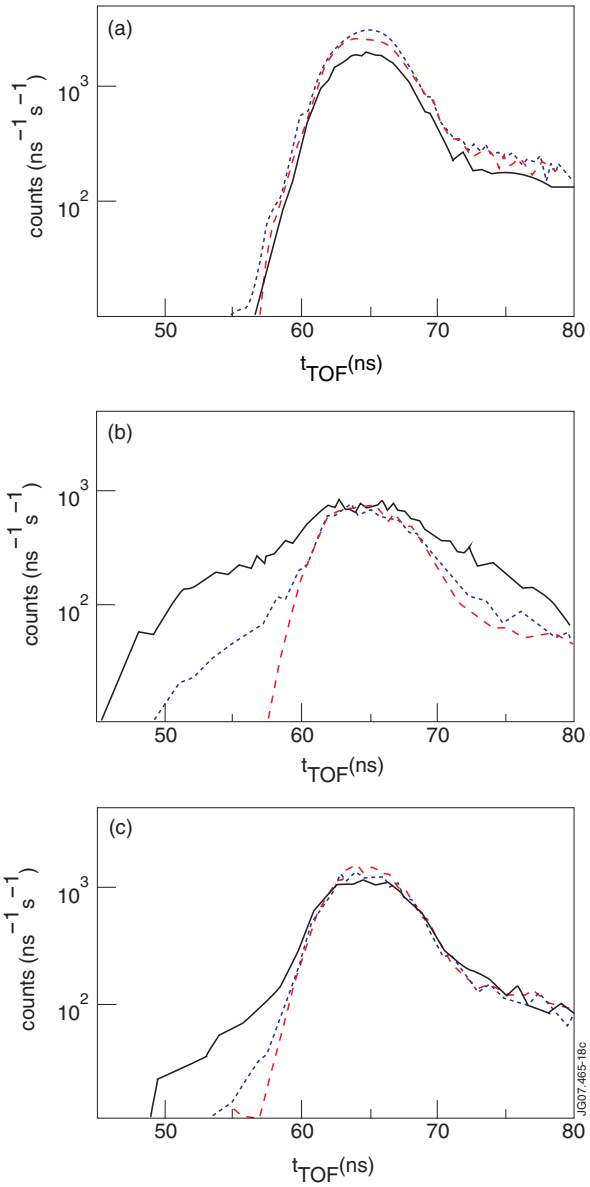

Figure 15. Neutron time of flight spectra (number of counts as function of flight-time—t_{TOF}) from the TOFOR neutron spectrometer. The top panel (*a*) shows data for pulse 69388 ($X[^3\text{He}] = 10$–12%: minority heating regime), the middle (*b*) and bottom (*c*) panels correspond to pulses 69392 and 69393 ($X[^3\text{He}] = 18\%$: mode conversion regime). Each panel displays spectra for three different contiguous time slices during the magnetic field flat top: short dashes for $t = 5$–6 s, long dashes for $t = 6$–7 s, solid lines for $t = 7$–8 s. The statistical uncertainties follow Poisson statistics, i.e. 100 counts give a 10% and 1000 counts a 3.2% accuracy.

reveal if the ^{3}He + D reaction is taking place alongside the D + D reaction. But grouping the information obtained from the various neutron diagnostics allows one to attest with more certainty what happens in the plasma. As high-energy neutrons are faster, they contribute counts on the short time-of-flight side of the spectrum, i.e. for $t_{TOF} < 65$ ns; correspondingly, neutrons with lower energies are found at $t_{TOF} > 65$ ns. For 69388, the ^{3}He concentration

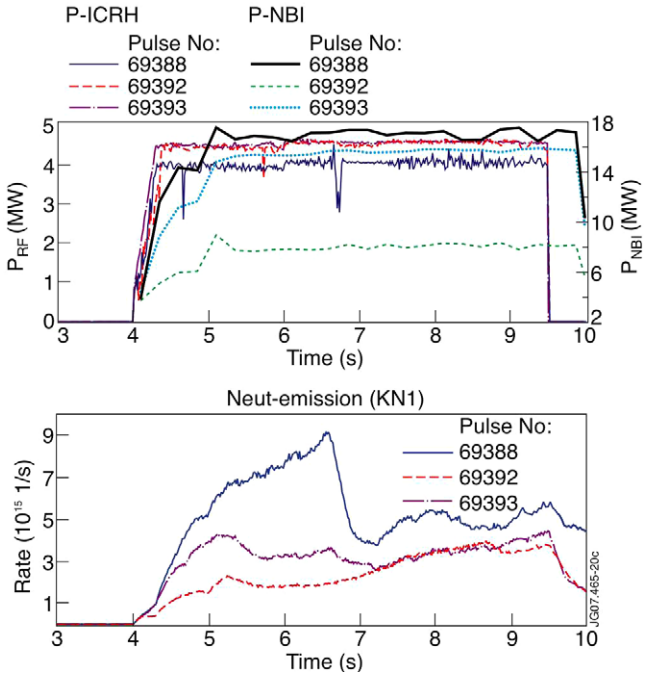

Figure 16. ICRH and NBI power (top) as well as neutron yield (bottom) as a function of time for shots 69388 (minority heating regime), 69392 and 69393 (mode conversion regime).

was $X[^3\text{He}] = 10$–12% (minority heating regime) while for 69393 it was $X[^3\text{He}] = 18\%$ (mode conversion regime); shot 69392 is similar to shot 69393 except that the NBI power was 8 MW (all by 130 keV injectors), while that of 69393 was 16 MW (half from 80 keV, half from 130 keV injectors). In each of the sub-figures of figure 15, the TOFOR spectra are given for three different contiguous time windows during the magnetic field flat top: short dashes are for $5 - 6s$, long dashes for 6–7 s, and solid lines are for 7–8 s. Note also that, in spite of having similar auxiliary heating powers, the number of TOFOR counts is smaller for 69393 than for 69388, an observation that is consistent with the total neutron yield measurement given by JET's standard neutron monitor diagnostic, the KN1 fission chamber system (see bottom figure of figure 16). Whereas the shape of the spectra for the main (65 ns) peak are similar for 69388 and 69393, a clear high-energy neutron tail is emerging as time progresses for 69393 while it is absent in the 69388 data. From a more detailed analysis of the TOFOR data it is seen that the high-energy neutron tail in the mode conversion regime pulse (69393) corresponds to a high-energy deuterium tail whose temperature exceeds 300 keV around $t = 9$ s. And although having only half the NBI heating power, mode conversion regime pulse 69392 gives rise to even more significant tails from fast deuteron ions. Evidence of the formation of the tail is equally observed in the KR2 low energy neutral particle analyzer (see figure 17) [45]: whereas the neutral particle flux is very similar for both discharges in the early phase of the discharge, a tail is clearly visible in mode conversion shots 69392 and 69393 later in the discharge, while it is absent in shot 69388.

A first attempt to model the effect of RF heating on the D beam ions was discussed in the theory section on Fokker–Planck modeling of this paper. Since ^{3}He was used as a minority gas and the RF frequency was chosen to favor core ^{3}He fundamental cyclotron resonance heating, one would expect tails being formed in these (^{3}He)–D plasmas to be fast ^{3}He ions.

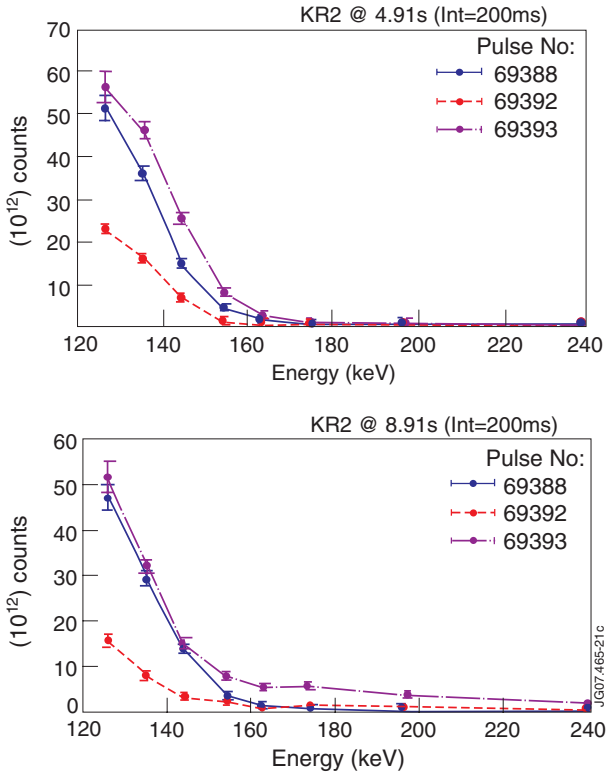

Figure 17. KR2 low energy neutral particle analyzer count spectra for shots 69388, 69392 and 69393 at $t = 4.9$ s (top) and at $t = 8.9$ s (bottom).

But in the mode conversion regime, the minority concentration is much too high for such ^{3}He tails to form, and the data analysis revealed that the fast particles were deuterons rather than ^{3}He. The combined use of RF and NBI heating is thought to be the key to understanding the D tail formation, as already suggested in [26] based on a resonance location analysis: with a thermal background, the deuterons hardly feel the presence of the RF fields since $\omega = \Omega_D$ is at $R = 2.4$ m i.e. about 0.6 m away from the core ($\omega = \Omega_{^3He}$ is at $R = 3.21$ m) and thus large RF power levels would be required to drive tails starting from thermal bulk D ions in this relatively cold region. Because JET is equipped with 80 and 130 keV beams, the Doppler-shifted resonance for NB injected D particles is however shifted up to $\approx$0.4 m towards the core. Moreover, being well away from the cold plasma cyclotron resonance $\omega = \Omega_D$ the beam particles do not suffer from the adverse polarization which normally makes fundamental cyclotron heating of a majority species poor. Being Doppler-shifted towards the center where the collisionality is significantly lower than in the plasma edge, higher energy Deuterium tails can be formed for a given RF power level. At the time of the first mode conversion experiments, no sufficiently sophisticated wave+Fokker–Planck modeling tools were available to quantitatively substantiate the role of the Doppler shift and study the formation of non-Maxwellian tails self-consistently. The more recent modeling indicates that—when tuning the RF frequency and/or the magnetic field to ensure core ^{3}He heating—the RF absorption of the beam ions is maximal at $\rho \approx 0.4$ m i.e. both well away from the cold plasma resonance (at $\rho \approx 0.6$ m) and the location at which the neutral beam particles are dominantly ionized (at $\rho \approx 0.2$ m). The presence of various competing effects suggests that conclusions on the

radial as well as velocity distribution of particles should be drawn with care. One intriguing hypothesis is the one proposed by Nguyen *et al* —be it in different circumstances—namely that heating at half harmonics might play a role [46]. Further analysis, outside the scope of this paper, is ongoing.

The experiments discussed here were performed in plasmas with transport barriers and were meant to shed light on the transport in such plasmas (see next section). Unlike the pronounced maximum of the neutron yield as a function of time in the minority heating discharge, the tail formation in the mode conversion shots is not a consequence of the ITB: looking at the ion temperature (not shown), at best a weak ITB was formed in shot 69393; at the time the tail is most developed the ion temperature is also lower both than the temperature at the same time in shot 69388 and at the time at which the ITB is most pronounced. As Mantsinen's experiments were performed in L-mode [26] rather than in an ITB plasma, it is clear that the D tail formation in (^{3}He)–D plasmas is not connected to ITB physics. As can be anticipated from the requirement that the ^{3}He heating needs to be small for the D tail to form, the observed effect does not even seem to directly depend on the presence of ^{3}He either: more recently, the beneficial synergistic effect of the simultaneous application of RF and NBI heating of a pure D plasma on the bulk ion temperature and on the neutron rate was shown to be equally due to the absorption of D beam ions at their Doppler-shifted resonance [17]. Both in the majority D experiments and (^{3}He)–D experiments two effects need to be noted: aside from the formation of the tail, the 'preheating' of the plasma by the beam contributes to an enhanced neutron rate, the latter due to a modification of the beam density due to a modification of the slowing down time via the collisionality.

8. Probing ITBs using RF power

Aside from ensuring plasma heating, RF heating can be used as a tool for probing plasmas (see, e.g. [47] for some examples). In this section an example is given of how it can be used to help understand the dynamics of plasmas with internal transport barriers. Various authors have studied ITBs, both for what concerns the excitation as their sustainment. The interested reader can e.g. refer to [48, 49] for an in depth discussion. In the last few JET campaigns the determination of the characteristics of ITBs was the main aim of the transport studies performed in (^{3}He)–D plasmas [23, 50, 51]. The transport analysis of the ITB plasmas aimed at answering two very specific questions:

- Is the improved confinement associated with an (electron) ITB limited to the narrow layer where the temperature is steepening, or is the improved confinement a characteristic of the whole region radially inside the transport barrier?
- Is an ITB a region in which transport is stiff and characterized by a threshold gradient that is larger than in conventional plasmas, or is it a region below threshold where turbulence is suppressed?

The answer to the first question is clear when looking at figure 18 in which (*a*) the ion as well as electron temperature of JET shot 59397 is depicted together with the density profile and the (strongly inverted) q-profile, and (*b*) the amplitude and phase of the fundamental electron temperature Fourier component responding to a modulation of the RF power is shown. In this case the dominant heating is mode conversion electron heating at the ITB position. One observes clear breaks in the slopes both of the amplitude and the phase of the fundamental ($N = 1$) temperature response at the foot and the top of the barrier, suggesting that the ITB layer itself is a narrow layer at which the diffusivity is lower than in the neighboring regions. Modeling shows that the diffusivity inside the ITB is actually an order of magnitude lower

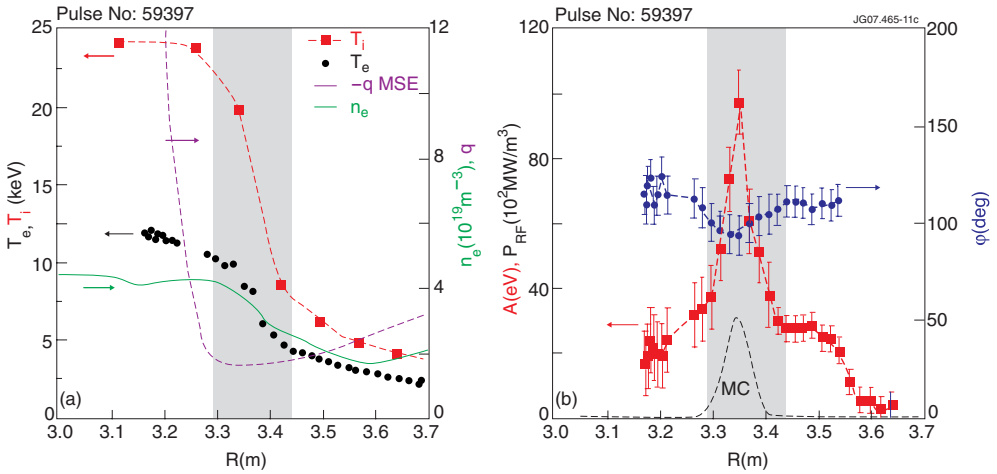

Figure 18. Transport analysis of ITB shot 59397 (reproduced from [23]) showing various quantities as a function of the major radius: (*a*) deeply reversed q-profile, density, ion and electron temperature profiles, (*b*) amplitude and phase of the fundamental Fourier component as well as the power deposition profiles adopted in the simulation. Reprinted figure with permission from Mantica *et al* [23]. Copyright (2006) by the American Physical Society.

than outside it. In the region radially inside the ITB the transport is not reduced; temperature response profiles obtained with the assumption that the whole core region is a region in which the diffusion coefficient is strongly reduced are at variance with experimental findings. Hence, ITBs are local phenomena that do not extend to the core, although the macroscopic quantities (such as density and temperature) are increased in the whole region inside the barrier and do depend on the ITB strength.

The answer to the second question was found by studying discharges having heat sources both inside and outside but not at the ITB. In that case the heat fronts very quickly disappear as soon as they penetrate the ITB (no graph shown; see [23]). This observation is interpreted as being due to a complete loss of stiffness i.e. as a plasma that becomes sub-critical to anomalous transport, the threshold being higher than conventional when inside the ITB. A more detailed analysis [23, 50] reveals that the amplitudes and phases of the temperature response are not symmetrical inside the ITB meaning that the diffusion is not uniform: R/L_{T_e} (L_{T_e} being the temperature gradient length) seems well below the threshold on the inner ITB while it stays closer to the threshold on the outer ITB side, meaning the ITB is more fragile at its foot than at its top.

A number of exotic phenomena were also identified when studying transport in presence of ITBs [51]. Commonly the amplitude and phase are extremal at the heat source. This is not necessarily the case in ITBs where an apparent convection can cause the maximal temperature response to be displaced from the source. Another unexpected phenomenon is that, in spite of there being only one heat source, a second maximum in the perturbation amplitude is sometimes generated close to the ITB foot. One of the maxima is linked to the actual mode conversion electron heat source. No second heat source (e.g. due to minority heating) is present to explain the supplementary maximum and conventional transport models do not permit to shed light on why such a second maximum can appear either. Casati *et al* showed that the critical gradient model offers a possible explanation of both phenomena [51].

9. RF power injection and impurity profile control in JET plasmas

To maximize the reactivity of a fusion plasma, the fuel dilution should be kept to a minimum. In particular, the impurity level should be kept as low as possible in the plasma core where the temperature is closest to that needed to trigger spontaneous fusion. Over the last few years both experimental and theoretical evidence has been accumulated that RF power—and more specifically power transferred to the electrons not too far from the plasma center—may flatten the impurity density profiles [52, 53]. This observation suggests that RF heating may be a natural candidate for removing undesirable species from the plasma. Recent (^{3}He)–D experiments relying on RF heating [54, 55] have added further evidence to strengthen the confidence in this conclusion.

The beneficial effect of electron heating on impurities was first noticed on ASDEX-Upgrade [56] using ECRH. In JET H-mode and Hybrid (^{3}He)–D discharges at ITER relevant collisionalities ($\nu_{\rm eff} < 0.2$), comparing discharges with and without RF power applied to the electrons, and transiently doped with traces of several impurities (Ne, Ar, Ni and Mo) were studied. For all of the injected impurities the so-called 'peaking factor' or 'pinch parameter' (i.e. the ratio of the convection velocity v and the diffusion D) experiences a remarkable reduction or even a sign reversal when RF power is applied to heat electrons; in steady state and in absence of internal impurity sources, the net particle flux is zero and thus $(\nabla N_{\rm imp})_\rho / N_{\rm imp} = v/D$ holds so v/D can be estimated from looking at the density. Correspondingly the impurity profiles are flattened or even become hollow [55]. The findings in (^{3}He)–D plasmas are consistent with those obtained in (H)–D plasmas: studies in (H)–D plasmas revealed that minority heating—predominantly heating the electrons as well, be it indirectly via the collisional slowing down of the minority ions—triggers the same impurity evacuation. On the other hand, minority heating experiments involving ^{3}He as a minority tend to show the opposite tendency, and result in strong impurity peaking in the core. One might surmise that the different behavior results from the fact that ^{3}He minority heating affects the ion rather than the electron channel. Already in 2006, a plausible pinch mechanism connected with the parallel velocity fluctuations was proposed to explain the experimentally observed change of the particle pinch direction when going from an ion to an electron heating scheme [57]. More recently it was confirmed that unstable modes rotating in the electron diamagnetic direction (TEMs or trapped electron modes), excited in the central region of the plasma by strong electron heating and generated by the non-adiabatic response of passing electrons, can induce an outward convection of the impurities [58].

10. Summary

This paper gives a preliminary and hence incomplete summary of key results obtained in recent JET experiments in deuterium plasmas containing a minority of ^{3}He gas and in which RF heating played a crucial role. Depending on the minority concentration different phenomena are observed.

At very low concentrations ($X[^3\text{He}] \leqslant 1\%$) and adopting core ion heating, fast ^{3}He tails are formed. Threshold fusion reactions creating high energy gamma rays and fast ion losses allow one to deduce that the tails have an effective temperature of a few hundred kiloelectronvolts. RF power is indispensable in this process: energetic ion losses as well as MHD modes depending on fast particle populations for their birth correlate with presence or absence of a sufficiently high level of launched power. Gamma ray tomography testifies for changes of the fast ion population distribution when sawtooth crashes occur.

At higher concentrations ($X[^3\mathrm{He}] \sim 8$–10%) ion heating is dominant and MHD activity is much reduced. Nevertheless, at best minority tails of moderate energy are observed in view of the mass of ^{3}He. At even higher concentrations, mode conversion heating becomes the dominant heating process and fast ^{3}He ions are absent. Absorption efficiencies inferred from analyzing the temperature response to modulations of the RF power demonstrate the switch-over from dominant ion heating—characterized by indirect electron and ion heating—to the mode conversion regime, WHERE direct wave absorption by the electrons is dominant. The location where the dominant absorption takes place agrees with that of theoretical predictions. Studying the electron response to RF power modulations allowed to experimentally observe the standing wave effect predicted by Fuchs *et al* [11].

Although the D cyclotron layer was far off-axis, high-energy RF heated D beam particles were observed in the mode conversion regime with the ^{3}He cyclotron layer lying in the plasma center. The simultaneous application of both RF and NBI heating is crucial to observe this tail, which is interpreted as being caused by the Doppler-shifted ICRF absorption of the beam Deuterons, which positions the absorption much more central than is the case for thermal D ions.

Plasmas with internal transport barriers were probed using localized RF heating. ITBs were identified as regions with reduced diffusivity. They are more fragile at their foot and allow exotic transport phenomena (such as a double maximum of the temperature response in the presence of a single heat source) to occur.

Finally, the present know-how on the potential of RF power—depending on whether the electrons or bulk ions are dominantly heated—to induce core impurity removal or accumulation was summarized.

Acknowledgments

This work has been conducted under the European Fusion Development Agreement. The views and opinions expressed herein do not necessarily reflect those of the European Commission.

References

[1] Van Eester D *et al* 2002 *Nucl. Fusion* **42** 310–28
[2] Start D *et al* 1998 *Phys. Rev. Lett.* **80** 4681–4
[3] Mayoral M-L *et al* 2006 *Nucl. Fusion* **46** S-550–S-563
[4] Lerche E *et al* 2007 *Proc. 17th Top. Conf. on RF Power in Plasmas (Clearwater, FL) AIP Conf. Proc.* **933** 47–50
[5] Noterdaeme J-M *et al* 2008 *Fusion Sci. Technol.* **53** 1103–151
[6] Van Eester D *et al* 1998 *Plasma Phys. Control. Fusion* **40** 1949–75
[7] Wright J C *et al* 2004 *Phys. Plasmas* **11** 2473–9
[8] Jaeger E F, Berry L A, Myra J R, Batchelor D B and Azevedo E D 2003 *Proc. 15th Topical Conf. on Radio Frequency Power in Plasmas (Moran, WY)* ed C B Forest *AIP Conf. Proc.* **694** 475–8
[9] Popovitch P 2004 Low frequency electromagnetic wave propagation in 3D plasma configurations *PhD Thesis* no 3063 CRPP, EPFL, Lausanne, Switzerland
[10] Vdovin V L 2005 ICRF benchmarking modelling of ITER scenario # *27th Steady State Operation ITPA Topical Group Meeting (Como, Italy, 4–6 May 2005)*
[11] Fuchs V *et al* 1995 *Phys. Plasmas* **2** 1637–47
[12] Stix T H 1992 *Waves in Plasmas* (New York: AIP)
[13] Van Eester D 2001 *J. Plasma Phys.* **65** 407–52
[14] Lamalle P U 1994 *PhD thesis* Université de Mons, *LPP-ERM/KMS Laboratory Report* 101
[15] Lamalle P U 1997 *Plasma Phys. Control. Fusion* **39** 1409–60
[16] Lerche E *et al* 2007 *Proc. 17th Top. Conf. on RF Power in Plasmas (Clearwater, FL) AIP Conf. Proc.* **933** 51–4

[17] Lerche E *et al* 2009 *Plasma Phys. Control. Fusion* **51** 044006
[18] Hedin J, Hellsten T, Eriksson L-G and Johnson T 2002 *Nucl. Fusion* **42** 527–40
[19] Murakami S *et al* 2005 *Natl Inst. Fusion Sci.* **808** 247–54
[20] Choi M *et al* 2003 *AIP Conf. Proc.* **694** 86–9
[21] Koch R 2006 *Proc. Carolus Magnus Summer School (Mechelen, The Netherlands) Fusion Sci. Technol.* **49** 187–94
[22] Lerche E *et al* 2008 *Plasma Phys. Control. Fusion* **50** 035003
[23] Mantica P *et al* 2006 *Phys. Rev. Lett.* **96** 0950020
[24] de la Luna E *et al* 2004 *Rev. Sci. Instrum.* **75** 3831–3
[25] von Hellermann M G 1990 *Rev. Sci. Instrum.* **61** 3479–86
[26] Mantsinen M 2004 *Nucl. Fusion* **44** 33–46
[27] Gowers C *et al* 2001 High resolution Thomson scattering on JET an assessment of the feasibility *Report* EFDA-JET-PR(01)29
[28] Krasilnikov A *et al* 2009 *Plasma Phys. Control. Fusion* **51** 044005
[29] Garbet X *et al* 2004 *Plasma Phys. Control. Fusion* **46** 1351–73
[30] Van Eester D *et al* 2003 *Proc. 15th Top. Conf. on RF Power in Plasmas (Moran, WY) AIP Conf. Proc.* **694** 66–73
[31] Mc Guire K *et al* 1983 *Phys. Rev. Lett.* **50** 891
[32] White R B *et al* 1983 *Phys. Fluids* **26** 2958
[33] Chen L, White R B and Rosenbluth M N 1984 *Phys. Rev. Lett.* **52** 1122
[34] Sharapov S E *et al* 2001 *Phys. Lett.* A **289** 127
[35] Kiptily V *et al* 2008 Recent progress in fast-ion physics on JET *Proc. 22nd IAEA Fusion Energy Conf. (Geneva, Switzerland, 13–18 October 2008)* Paper EX/P8-8
[36] Kiptily V *et al* 2002 *Nucl. Fusion* **42** 999–1007
[37] Cheng C Z *et al* 1985 *Ann. Phys. (NY)* **161** 21
[38] Bergkvist T *et al* 2005 *Nucl. Fusion* **45** 485–93
[39] Darrow D *et al* 2006 *Rev. Sci. Instrum.* **77** 10E701
[40] Sandquist P *et al* 2007 Bi-directional tornado modes on JET *JET Report* EFDA-P(07)25
Sandquist P *et al* 2007 *Phys. Plasmas* **14** 122506
[41] Johnson T *et al* 2003 *Proc. 14th Top. Conf. on RF Power in Plasmas (Oxnard, CA) AIP Conf. Proc.* **595** 102–5
[42] Sharapov S *et al* 2004 *Phys. Rev. Lett.* **93** 165001
[43] Hjalmarsson A *et al* 2003 *Rev. Sci. Instrum.* **74** 1750–2
Kallne J *et al* 2004 Advanced neutron diagnostics for ITER fusion experiments *Report* EFDA-JET-CP(04)07-19
[44] Hellesen C *et al* 2007 Measurement and analysis of the neutron emission from RF and NB heated JET D plasmas using the TOFOR spectrometer Report EFDA-JET-CP(07)03/47
Giacomelli L *et al* 2007 Neutron emission spectroscopy diagnosis of fast ions in RF heated $D-(^3\mathrm{He})$ plasmas at JET *Proc. 34th EPS Conf. (2–6 July 2007, Warsaw, Poland)* ECA vol 31F P-2.134
[45] Korotkov A A *et al* 1997 *Nucl. Fusion* **37** 35–51
[46] Nguyen F *et al* 2002 *Proc. 29th EPS Conf. on Plasma Physics (Montreux, Switzerland)* vol 26B (ECA) P-1.045
[47] Mantsinen M *et al* 2003 *Plasma Phys. Control. Fusion* **45** A445–56
[48] Joffrin E *et al* 2002 *Nucl. Fusion* **42** 235–42
[49] Tala T and Garbet X 2006 *C. R. Physique* **7** 622–33, also *Jet Reports* EFDA-JET-PR(06)08
[50] Marinoni A *et al* 2006 *Plasma Phys. Control. Fusion* **48** 1469–87
[51] Casati A *et al* 2007 *Phys. Plasmas* **14** 092303
[52] Puiatti M E *et al* 2006 Analysis of metallic impurity density profiles in low collisionality JET H-Mode and L-Mode plasmas *Report* EFDA-JET-PR(05)46
Puiatti M E *et al* 2006 *Phys. Plasmas* **13** 042501
[53] Giroud C *et al* 2006 Progress in understanding of impurity transport at JET *Report* EFDA-JET-CP(06)05-21
Giroud C *et al* 2006 *Proc. 21st IAEA Fusion Energy Conf. (Chengdu, China, 16–22 October 2006)*
[54] Valisa M *et al* 2007 Effect of radio-frequency power injection on impurity profile in JET plasmas *49th Annual Meeting of the Division of Plasma Physics (DPP) (Orlando, FL, November 2007)*
[55] Carraro L *et al* 2007 Impurity profile control in JET plasmas with radio-frequency power injection *34th EPS Conf. (Warsaw, Poland)* also *Report* EFDA-JET-CP(07)03/05
[56] Dux R *et al* 2003 *Plasma Phys. Control. Fusion* **45** 1815–25
[57] Angioni C *et al* 2006 *Phys. Rev. Lett.* **96** 095003
[58] Angioni C *et al* 2007 *Plasma Phys. Control. Fusion* **49** 2027